



## Insight into efficient degradation of 3,5-dichlorosalicylic acid by Fe-Si-B amorphous ribbon under neutral condition

Libo Zhang<sup>a</sup>, Lianxiang Qiu<sup>a</sup>, Qingyao Zhu<sup>b</sup>, Xiong Liang<sup>a</sup>, Jingxiong Huang<sup>b</sup>, Mengting Yang<sup>b</sup>, Zhenxuan Zhang<sup>a,\*</sup>, Jiang Ma<sup>a,\*</sup>, Jun Shen<sup>a</sup>

<sup>a</sup> College of Mechatronics and Control Engineering, Shenzhen University, Shenzhen, 518060, PR China

<sup>b</sup> College of Chemistry and Environmental Engineering, Shenzhen University, Shenzhen, 518060, PR China

### ARTICLE INFO

#### Keywords:

Amorphous alloy ribbon  
Disinfection by-products  
3,5-Dichlorosalicylic acid  
Fenton-like reaction  
High-valent iron

### ABSTRACT

Water disinfection would result in unintended formation of halogenated disinfection by-products (DBPs) which pose potential harm to human health. In present work, Fe<sub>78</sub>Si<sub>9</sub>B<sub>13</sub> amorphous ribbons (Fe-Si-B<sup>AR</sup>) showed excellent catalytic degradation performance towards an aromatic DBP, 3,5-dichlorosalicylic acid (3,5-DiClSA) by Fenton-like reaction. The catalytic degradation performances of Fe-Si-B<sup>AR</sup>, Fe<sub>78</sub>Si<sub>9</sub>B<sub>13</sub> crystalline ribbons (Fe-Si-B<sup>CR</sup>) and iron powders towards 3,5-DiClSA were compared, and Fe-Si-B<sup>AR</sup> (0.0166 min<sup>-1</sup>) showed the fastest degradation rate. The faster surface mobility of Fe-Si-B<sup>AR</sup>, which made it easy for Fe<sup>2+</sup> to be oxidized by H<sub>2</sub>O<sub>2</sub>, facilitated the degradation process. High-valent iron of Fe<sup>IV</sup> could be generated which accounted for degradation of 3,5-DiClSA. The Fe-Si-B<sup>AR</sup> also showed better and better catalytic performance in 10 reuse cycles. Besides, the cytotoxicity tests indicated that the overall toxicity level of 3,5-DiClSA was declined by 88.1 % after degradation by Fe-Si-B<sup>AR</sup>. Our results showed that Fe-Si-B<sup>AR</sup> is a promising catalyst for the degradation of aromatic DBPs.

### 1. Introduction

In the field of water treatment, drinking water increasingly becomes a hot topic since it directly relates to human health. As the greatest public health triumph, drinking water disinfection plays an important role in reducing the occurrence and death of infectious diseases caused by pathogenic microorganisms [1]. However, when disinfectant (chlorine) reacts with natural organic matter and/or bromine ion/iodine ion in water, disinfection by-products (DBPs) which pose potential harm to human health will be generated in drinking water [2]. Epidemiological studies have illustrated that DBPs exposure potentially raises health risks, e.g., colorectal/bladder cancer and adverse birth outcomes [3]. Since trichloromethane was firstly detected in chlorinated drinking water in 1974, more than 700 kinds of DBPs have been identified successively [4]. Therefore, how to effectively control the generation of DBPs while at the same time ensuring disinfection became a challenging topic during drinking water treatment process. In recent years, new treatment processes such as ozone-activated carbon, membrane technology, zero-valent iron (ZVI), as well as advanced oxidation processes (AOPs) were proposed for advanced treatments [5]. AOPs including UV/O<sub>3</sub>, UV/H<sub>2</sub>O<sub>2</sub>, ZVI/persulfate received more attention due to their

broad-spectrum and high-efficiency removal effect, especially for the treatment of some recalcitrant pollutants [6]. As can be employed in multiple treatment choices, ZVI seems to become an ideal catalyst because of its reducibility, good environmental compatibility, low cost, and various degradation applications (dehalogenation reduction/combined with AOPs) [7–9]. However, due to the poor stability of iron powder itself, which make it easy to agglomerate, and the gradual accumulation of surface oxide layer during the reaction reduced the degradation efficiency, which largely limited its application in the removal of DBPs [10]. Through the modification of ordinary iron powder, such as the use of smaller size of nano ZVI, the specific surface area can be increased, which can greatly improve its ability of adsorption, reduction and degradation of pollutants. Unfortunately, the high cost and certain biological toxicity of nano ZVI will bring new environmental risks, which hindered its practical application as well [11]. As a special ZVI material with corrosion resistance, high catalytic activity, environmental friendliness and low cost, Fe-based amorphous alloys are expected to effectively solve this problem.

Amorphous alloys are new types of metal materials with short-range ordered and long-range disordered atomic structures [12]. They have attracted extensive attentions both in scientific and industrial areas

\* Corresponding authors.

E-mail addresses: [zxzhang@szu.edu.cn](mailto:zxzhang@szu.edu.cn) (Z. Zhang), [majiang@szu.edu.cn](mailto:majiang@szu.edu.cn) (J. Ma).

<https://doi.org/10.1016/j.apcatb.2021.120258>

Received 16 February 2021; Received in revised form 22 April 2021; Accepted 24 April 2021

Available online 26 April 2021

0926-3373/© 2021 Elsevier B.V. All rights reserved.

owing to their unique physical, chemical and mechanical properties [13–18]. In recent years, amorphous alloys have been used as environmental-friendly catalysts [19] in degradation of dye wastewater in water treatment field. Being employed in AOPs, e.g. Fenton-like reaction, the metastable nature of amorphous alloys brings them advanced catalytic and chemical properties which are unachievable for their crystalline counterparts [20,21]. Besides, the generation of reactive species such as hydroxyl radical ( $\cdot\text{OH}$ ) with relatively high redox potential ( $E^\circ = 2.7\text{--}2.8\text{ V}$ ) could effectively oxidize almost all kinds of organic pollutants including direct blue 6, methylene blue, acid orange II and convert them into  $\text{CO}_2$ ,  $\text{H}_2\text{O}$  and small inorganic molecules without discrimination [22]. Numerous works have been published regarding the degradation of dye wastewater by using amorphous alloys during the past decades [23–33]. In recent years, non-free radical high-valent iron such as  $\text{Fe}^{\text{IV}}$  can be found generated in some analogous Fenton-like reactions [34–38], which attracted much attention in the field of advanced oxidation considering that  $\text{Fe}^{\text{IV}}$  is capable of allowing selective oxidation whereas  $\cdot\text{OH}$  engages in uncontrolled oxidation [39]. Compared with the complex and huge amounts of chemical pollution problems in water environment, the catalytic degradation application of amorphous alloys is far from being fully developed.

Based on the above discussion, we propose to apply Fe-based amorphous alloys –  $\text{Fe}_{78}\text{Si}_9\text{B}_{13}$  amorphous ribbons ( $\text{Fe-Si-B}^{\text{AR}}$ ) into the degradation of one kind of aromatic halogenated DBPs – 3,5-dichlorosalicylic acid (3,5-DiClSA) since it has been frequently detected in drinking water with higher developmental toxicity than regulated aliphatic DBPs [40–42]. As it's been widely acknowledged that pH in real drinking water is almost from 6.5 to 8.5 [43]. Thus, the drinking water treatment normally carried out in neutral condition. The objects of this work are (1) to evaluate the catalytic degradation property and durability of  $\text{Fe-Si-B}^{\text{AR}}$  for 3,5-DiClSA by using Fenton-like reaction under neutral condition,  $\text{Fe}_{78}\text{Si}_9\text{B}_{13}$  crystalline ribbons ( $\text{Fe-Si-B}^{\text{CR}}$ ) and Fe powder were also selected to compare degradation performance and analyze the possible reasons; (2) to test whether toxicity level reduction coincide with chemical degradation; (3) to investigate surface property changes of  $\text{Fe-Si-B}^{\text{AR}}$  during degradation, as well as the mechanisms for degradation. The results of the present work are expected to provide an alternative advanced treatment for drinking water treatment under neutral condition, and to expand the functional application of Fe-based amorphous alloys.

## 2. Experimental

### 2.1. Materials

3,5-Dichlorosalicylic acid (3,5-DiClSA, >99 %) and  $\text{H}_2\text{O}_2$  (30 %, w/w) were purchased from Sigma-Aldrich. 5,5-dimethyl-1-pyrroline N-oxide (97 %), isopropanol (99.5 %), methyl phenyl sulfoxide (98 %), methyl phenyl sulfone (98 %), and  $\text{Na}_2\text{S}_2\text{O}_3$  (99 %) was bought from Aladdin. They were analytical grade and used as received without further purification. Preparation of  $\text{Fe}_{78}\text{Si}_9\text{B}_{13}$  amorphous ribbons ( $\text{Fe-Si-B}^{\text{AR}}$ ): The  $\text{Fe}_{78}\text{Si}_9\text{B}_{13}$  master ingot was synthesized by arc melting of mix of pure Fe, Si and B elements (>99.9 %) under Ti-gettered argon atmosphere. Then the master ingot was remelted in quartz tube by induction melting, followed by single-roller melt spinning to obtain  $\text{Fe-Si-B}^{\text{AR}}$  with thickness of  $26 \pm 1\ \mu\text{m}$ .  $\text{Fe-Si-B}^{\text{AR}}$  were vacuum-annealed at 873 K for 30 min to obtain  $\text{Fe}_{78}\text{Si}_9\text{B}_{13}$  crystalline ribbons ( $\text{Fe-Si-B}^{\text{CR}}$ ). Fe powder (1600 mesh, 99.9 % pure) was obtained from ZhongNuo Advanced Material (Beijing, China). Ultrapure water was used throughout the catalytic degradation experiments.

### 2.2. Characterization

X-ray diffraction analysis (XRD, Rigaku MiniFlex600) was performed to identify structure of the three materials. Their surface morphology and element information before and after degradation were observed

using a scanning electron microscope (SEM, FEI Quanta 450FEG) equipped with an energy dispersive spectrometer (EDS). X-ray photoelectron spectroscopy (XPS, Thermo Escalab 250XI) was used to further confirm the chemical status and composition of  $\text{Fe-Si-B}^{\text{AR}}$  before and after degradation.

### 2.3. General process of degradation experiments

Catalytic degradation experiments for 3,5-DiClSA by using  $\text{Fe-Si-B}^{\text{AR}}$ ,  $\text{Fe-Si-B}^{\text{CR}}$  and Fe powder were conducted. The initial pH of 3,5-DiClSA solution was measured by a digital pH meter (Mettler Toledo FE28). In a typical experiment, solutions of 3,5-DiClSA ( $1.2\ \mu\text{mol L}^{-1}$ ) were prepared by serial dilution from stock solution ( $20\ \text{mg L}^{-1}$ ), some specific amount of  $\text{H}_2\text{O}_2$  (w/w, 30 %) were then added into a 250 ml sample bottle and diluted to a total volume of 200 mL, after which some specific amount of ribbons/Fe powders were added into the solution as a catalyst. Then the solution was placed in a water bath for constant temperature during the reaction. Every 20 min, 3 ml 3,5-DiClSA solution was removed and filtered with  $0.22\ \mu\text{m}$  polyether sulfone (PES) membrane (Bojin, Tianjin) for measurement by using synchronous fluorescence spectroscopy [44] on a fluorescence spectrophotometer (PerkinElmer FL8500). The concentration of 3,5-DiClSA was directly calculated from synchronous fluorescence spectrums by selecting  $\Delta\lambda = 111\ \text{nm}$  as optimal condition (Fig. 1). Standard curve of 3,5-DiClSA with different concentrations (0.2, 0.4, 0.8, 1.2, 1.6, 2.0,  $2.4\ \mu\text{mol L}^{-1}$ ) were established (Fig. 1a) and linearity relationships could be found between concentration and the relative fluorescence intensity, as shown in Fig. 1b. For 3,5-DiClSA solution with an unknown concentration, its actual concentration can be calculated from its fluorescence intensity through the standard curve. As displayed in Fig. 1c–1f, the control and experimental group for chemical degradation processes of 3,5-DiClSA can be successfully monitored by using synchronous fluorescence spectroscopy. More details about the synchronous fluorescence method can be found in Figs. S1–S3, and Tables S1–S2 in Supporting Information (SI).

### 2.4. Analysis of reactive species by electron paramagnetic resonance (EPR)

EPR combined with spin trapping technology can be used for qualitative and quantitative detection of unpaired electrons in atoms or molecules, so as to detect reactive species [45]. EPR spectrometry was performed by using a Bruker EPR-E500 (Germany) instrument and 5,5-dimethyl-1-pyrroline N-oxide (DMPO) was selected as a spin-trapping reagent for reactive species. The detailed procedures for detection of real-time spin adducts are as follows:  $1380\ \mu\text{l}$  DMPO solution ( $145\ \text{mmol L}^{-1}$ ) and  $16\ \mu\text{l}$   $\text{H}_2\text{O}_2$  (30 %, w/w) were sequentially added to a 30 ml sample bottle. Then ultrapure water was added and diluted to 20 mL, and mixed solutions of DMPO (10 mmol/L) and  $\text{H}_2\text{O}_2$  (8 mmol/L) were obtained. Next, 0.08 g  $\text{Fe-Si-B}^{\text{AR}}$  were added into the solution and shaken slightly for 20 s to initiate the reaction. After being reacted for 5 min, 1 ml reaction solution was extracted into a 20 ml sample bottle and the bottle was shaken slightly for 2 min for full combination of DMPO and reactive species. A small amount of reaction solution was taken by a capillary tube, which was sealed at one end by vacuum grease and inserted into the EPR cavity for analysis. EPR detection was conducted at room temperature under the following detection parameters: center field of 3500 G, sweep width of 100 G, sweep time of 60 s, modulation frequency of 100 kHz, modulation amplitude of 1 G, microwave frequency of 9.63 GHz, and microwave power of 6.325 mW.

### 2.5. Mammalian cell cytotoxicity assay

Chinese hamster ovary (CHO)-K1 cells [46] were acquired from the American Type Culture Collection. Cells were grown in Ham's F12-K

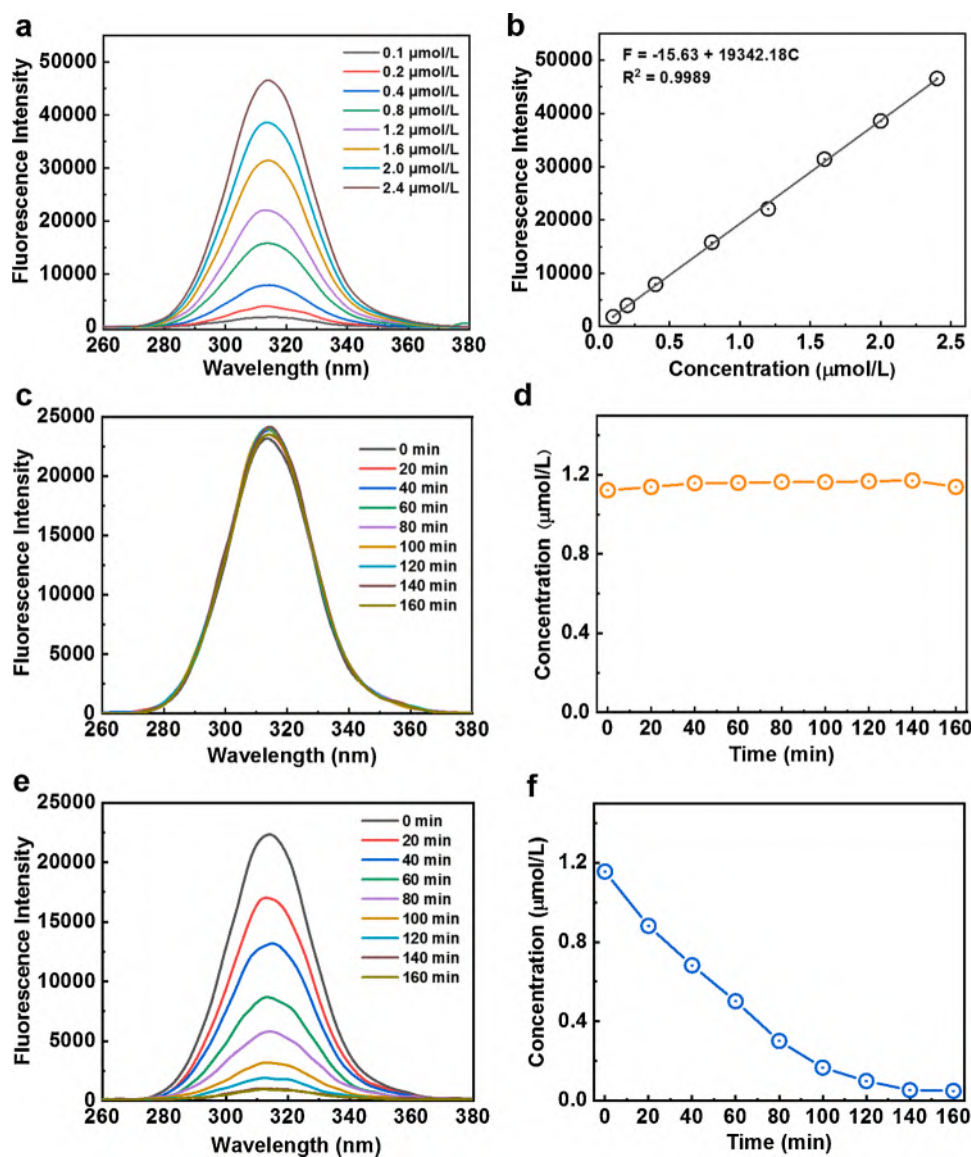


**Fig. 1.** (a) Fluorescence intensity of 3,5-DiClSA standard solution with different concentration; (b) Standard curve of 3,5-DiClSA solution; (c) Fluorescence intensity change of control group for degradation of 3,5-DiClSA; (d) Concentration change of 3,5-DiClSA in control group; (e) Fluorescence intensity change of 3,5-DiClSA during degradation process by Fe-Si-B<sup>AR</sup>; (f) Concentration change of 3,5-DiClSA during degradation process by Fe-Si-B<sup>AR</sup> (Ribbon dosage = 4 g L<sup>-1</sup>, pH = 7.0, T = 298 K, C<sub>3,5-DiClSA</sub> = 1.2 μmol L<sup>-1</sup>, C<sub>H<sub>2</sub>O<sub>2</sub></sub> = 4 mmol L<sup>-1</sup>).

medium (Hyclone) containing 5% fetal bovine serum (FBS, Hyclone) and 1% antibiotics (100 U/mL sodium penicillin G, 100 μg/mL streptomycin sulfate, 0.25 μg/mL amphotericin B, 0.85 % saline) at 37°C in a humidified atmosphere of 5% CO<sub>2</sub>. Detailed information for cytotoxicity measurement can be found in SI.

## 2.6. UPLC-ESI-tqMS analysis of PMSO and PMSO<sub>2</sub>

Whether high-valent iron such as Fe<sup>IV</sup> was generated in the degradation system can be tested by using methyl phenyl sulfoxide (PMSO) as the probe to see if it can be oxidized to methyl phenyl sulfone (PMSO<sub>2</sub>) through oxygen transfer reaction [34]. The concentration change of PMSO and PMSO<sub>2</sub> was measured by using ultra pressure liquid chromatography (UPLC) – electrospray ionization (ESI) – triple quadrupole mass spectrometry (tqMS) on a UPLC (Acquity I-class, Waters) coupled with ESI-tqMS (Xevo TQ-S micro, Waters) system in positive ionization mode. A BEH C18 (1.7 μm, 2.1 × 100 mm, Waters) at a column temperature of 35 °C was selected for UPLC separation. The mobile phase composed of water and methanol was set at a flow rate of 0.40 ml/min. The gradient was set at 5 % methanol and 95 % water initially and linearly changed to 90 % methanol and 10 % water in the first 8 min, followed by a quickly return in 0.1 min to 5 % methanol and 95 % water,

and then held for additional 2.9 min for re-equilibration. The parameters of ESI-tqMS were set as: cone voltage, 20 V; capillary voltage, 2.8 kV; collision energy, 15 V; source temperature, 150 °C; desolvation temperature, 400 °C; desolvation gas flow, 800 L/h; cone gas flow, 50 L/h; and collision gas (Ar) flow, 0.25 mL/min. Standard compounds of PMSO and PMSO<sub>2</sub> were used for structure confirmation and concentration monitoring (MRM).

## 2.7. DFT calculation

The adsorption energies ( $E_{\text{ads}}$ ) for three materials Fe-Si-B<sup>AR</sup>, Fe-Si-B<sup>CR</sup>, and Fe powder towards H<sub>2</sub>O<sub>2</sub> were calculated by using density functional theory (DFT) performed by Vienna Ab Initio Simulation Package (VASP) [47], based on the projector augmented wave (PAW) method within the generalized gradient approximation (GGA) [48]. The configurations of three kinds of materials were fully optimized. The exchange correlation potential was calculated by using revised Perdew-Burke-Ernzerhof (PBE) function [49,50] for solid systems (PBEsol) [51,52] in order to improve the equilibrium properties of solids [53]. PAW pseudopotentials were adopted for valence-core interactions calculation [54]. The Monkhorst-Pack grids of (3 × 3 × 1) were applied

for Brillouin zone sampling [48]. The parameters for cut off energy was set as 300 eV, the maximum force was set as  $0.002 \text{ eV \AA}^{-1}$ , the convergence tolerance of energy was set as  $1 \times 10^{-6} \text{ eV}$ , and the maximum displacement was set as  $0.002 \text{ \AA}$  [48], respectively.

### 3. Results and discussion

#### 3.1. Catalytic degradation performance of Fe-Si-B<sup>AR</sup> compared with Fe-Si-B<sup>CR</sup> and Fe powder

Fe-Si-B<sup>AR</sup>, Fe-Si-B<sup>CR</sup> and Fe powder (1600 mesh, 99.9 % pure) were selected to degrade 3,5-DiClSA (Fig. 2a) in order to compare their catalytic degradation performance under neutral condition. Their X-ray diffraction (XRD) patterns were shown in Fig. 2b. The degradation processes were non-destructively monitored by using synchronous fluorescence spectroscopy. In addition, 3D fluorescence spectrums of 3,5-DiClSA during the catalytic degradation by Fe-Si-B<sup>AR</sup> and Fe-Si-B<sup>CR</sup> were scanned for more visualized comparison and displayed in Fig. S4 in SI.

The reaction conditions were: ribbon/powder dosage =  $4 \text{ g L}^{-1}$ ,  $C_{3,5\text{-DiClSA}} = 1.2 \text{ \mu mol L}^{-1}$ ,  $\text{pH} = 7.0$ ,  $T = 298 \text{ K}$ , and  $C_{\text{H}_2\text{O}_2} = 4 \text{ mmol L}^{-1}$ . According to Fig. 2c, the residual concentration percentage of 3,5-DiClSA by Fe-Si-B<sup>AR</sup>, Fe-Si-B<sup>CR</sup> and Fe powder reached 5.0 %, 48.9 % and 95.9 % after 160 min of catalytic degradation process, respectively. The average values were presented and error bars represent the range of three replicate samples. Almost no 3,5-DiClSA degradation occurred in the experimental group added with Fe powder. All the degradation

processes followed the pseudo-first-order kinetic model:

$$C_t/C_0 = \exp(-kt) \quad (1)$$

where  $k$  is the reaction rate constant and  $t$  is the degradation time. Exponential model was applied to fit the data. Fitting results showed that reaction rate constant of Fe-Si-B<sup>AR</sup> was  $0.0166 \text{ min}^{-1}$ , which was higher than  $0.0040 \text{ min}^{-1}$  for Fe-Si-B<sup>CR</sup> and significantly higher than  $0.0006 \text{ min}^{-1}$  for Fe powder, indicating that the homogeneous amorphous structure benefited to the catalytic degradation performance of the ZVI. The comparison of degradation processes by Fe-Si-B<sup>AR</sup> and Fe-Si-B<sup>CR</sup> can be observed more directly from 3D fluorescence spectra in Figs. S4a, and S4b, respectively. The specific fluorescence peak of 3,5-DiClSA appeared at the excitation wavelength of 314 nm and emission wavelength of 425 nm, whose color was yellow at 0 min. As time advanced, the peak's color changed to dark blue, indicating that 3,5-DiClSA was almost completely degraded after 120 min. In contrast, the color change of the peak of 3,5-DiClSA degraded by Fe-Si-B<sup>CR</sup> was much slower (Fig. S4b). These results demonstrated that Fe-Si-B<sup>AR</sup> had the best catalytic degradation performance for 3,5-DiClSA among the three materials under neutral condition.

#### 3.2. Cytotoxicity analysis of 3,5-DiClSA solution before and after degradation

Fe-Si-B<sup>AR</sup> showed best performance among the three materials for chemical degradation, while the question raised up as whether toxicity level decreased or not after degradation? In case the toxicity level did

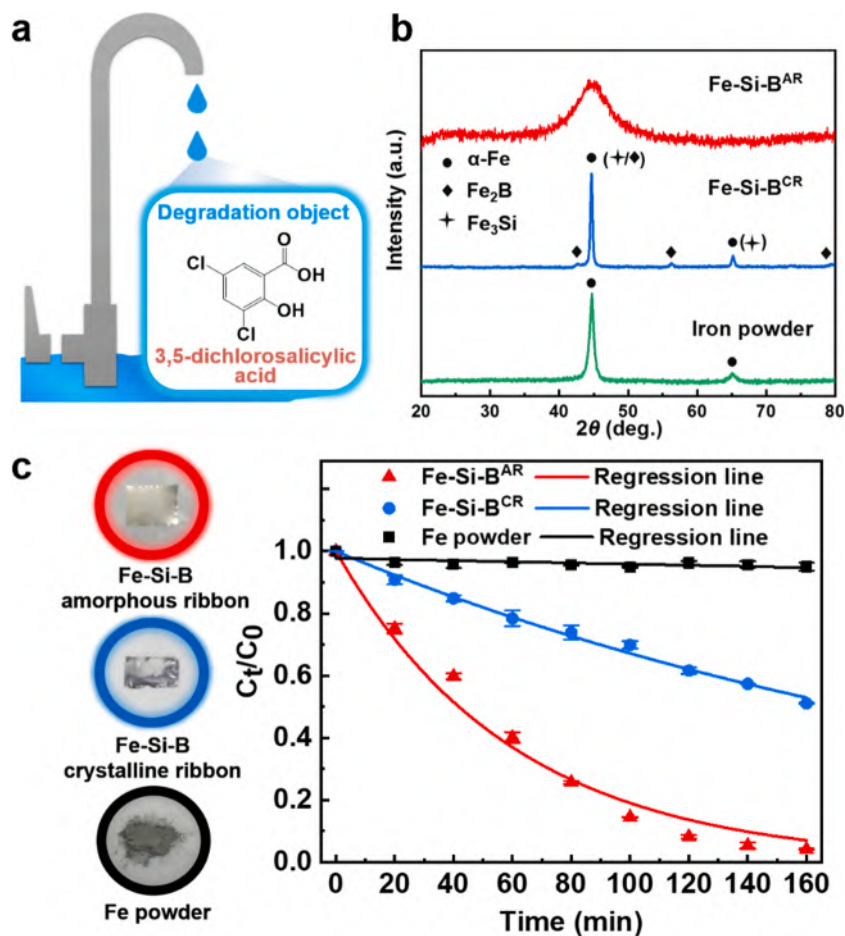


Fig. 2. (a) Degradation target in this work; (b) XRD patterns of original Fe-Si-B<sup>AR</sup>, Fe-Si-B<sup>CR</sup> and Fe powder; (c) Normalized concentration change of 3,5-DiClSA during degradation process by Fe-Si-B<sup>AR</sup>, Fe-Si-B<sup>CR</sup> and Fe powder and fitting curves (Ribbon/Powder dosage =  $4 \text{ g L}^{-1}$ ,  $\text{pH} = 7.0$ ,  $T = 298 \text{ K}$ ,  $C_{3,5\text{-DiClSA}} = 1.2 \text{ \mu mol L}^{-1}$ ,  $C_{\text{H}_2\text{O}_2} = 4 \text{ mmol L}^{-1}$ ).

not show the performance as good as for chemical degradation, e.g. some of the metabolites had relatively higher toxic potency, the practical application of the catalysts have to be reassessed. Cytotoxicity assay by using Chinese Hamster Ovary (CHO)-K1 cells [46,55], which has been successfully used to measure toxicity level of individual DBP or overall toxicity level of water samples was adopted to test toxicity changes of 3,5-DiClSA before and after degradation. The lethal concentration 50 value ( $LC_{50}$ ), which is the concentration of a toxic that will lead to the 50 % deaths of the cells tested, is a factor that can be used to indicate toxic potency [55]. For overall cytotoxicity measurement of water samples, concentration processes were normally needed before exposure. Thus, concentration factor was frequently used as the unit to indicate  $LC_{50}$  [56]. In the present study, the initial degradation concentration for 3,5-DiClSA is  $1.2 \mu\text{mol L}^{-1}$ , as displayed in Fig. 3, the results showed that the calculated  $LC_{50}$  before and after degradation by Fe-Si-B<sup>AR</sup> was 397 times and 3350 times of initial degradation concentration. The latter value was 8.4 times as high as the former, indicating the cytotoxicity level in the 3,5-DiClSA solution after degradation by Fe-Si-B<sup>AR</sup> decreased by 88.1 % compared with the original solution.

### 3.3. Characterization of materials before and after degradation

The surface morphology changes of the three materials before and after the degradation process were carried out to confirm how active they participated in the catalytic degradation. Fig. 4a–4f showed surface morphology of three materials before and after degradation process. The surface of Fe-Si-B<sup>AR</sup> and Fe-Si-B<sup>CR</sup> before degradation process were nearly perfectly smooth with no apparent defects as well as the Fe spherical particles. After degradation process, the surface morphologies of the three materials showed obvious differences to varying degrees, among which a layer of sediments was attached to the Fe-Si-B<sup>AR</sup> surface. After removing the sediments, a pit-shaped reaction area could be clearly seen in Fig. 5a. Such pits were also found in study of Chen et al. on degradation of azo dye by Fe-based amorphous alloy [57]. There were slight changes on the surface of Fe-Si-B<sup>CR</sup>, with no sediments as attachment and only a few micropores. The surface of Fe powder remained smooth and had no obvious changes compared with that before degradation process, as can be seen in Fig. 4c and 4f. The surface morphology changes reflected that Fe-Si-B<sup>AR</sup> took the most active participation in the degradation process, which also explained why Fe-Si-B<sup>AR</sup> had the best catalytic performance in degradation of 3,5-DiClSA.

Besides the changes of surface morphology, the change of Fe atom content in Fe-Si-B<sup>AR</sup> also attracted our attention. Fig. 5b and Table 1

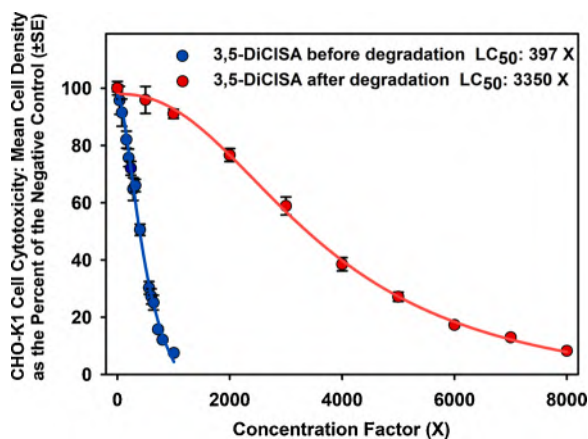


Fig. 3. Mammalian cell cytotoxicity assay: concentration-response curves of cytotoxicity of 3,5-DiClSA before and after degradation by Fe-Si-B<sup>AR</sup> (Ribbon dosage =  $4 \text{ g L}^{-1}$ , pH = 7.0,  $T = 298 \text{ K}$ ,  $C_{3,5\text{-DiClSA}} = 1.2 \mu\text{mol L}^{-1}$ ,  $C_{\text{H}_2\text{O}_2} = 4 \text{ mmol L}^{-1}$ ).

showed the energy dispersive spectrometer (EDS) results of original Fe-Si-B<sup>AR</sup> and pit-shaped reaction area on Fe-Si-B<sup>AR</sup> after degradation by one and ten reuse cycles. It can be calculated that the atom ratio of Fe to Si was 8.38:1 for original Fe-Si-B<sup>AR</sup>, which was very close to the nominal value expected for Fe-Si-B<sup>AR</sup>, in which the ratio was 78:9. After one and ten reuse cycles, the ratio decreased from 8.38:1 to 5.40:1 and continuously decrease to 3.48:1. In addition, EDS mappings of the pit reaction area and the intact area on Fe-Si-B<sup>AR</sup> after degradation process were shown in Fig. 5c and 5d, indicating that the Fe content in the pit area was significantly lower than that in the intact area. These results indicated that the content of Fe atom on the surface of Fe-Si-B<sup>AR</sup> decreased gradually, proving that Fe plays an important role in the catalytic degradation process.

To further understand the surface property changes, X-ray photoelectron spectroscopy (XPS) analysis was carried out for original and reused Fe-Si-B<sup>AR</sup> after one or ten degradation cycles, and the results were shown in Figs. 5e and 6. XPS peak at 710.2 eV represented Fe<sup>2+</sup>, and the summit of Fe<sup>2+</sup> peak increased after Ar etching by 2 nm. The proportion of the area for Fe<sup>2+</sup> peak to the total area of Fe 2p peak is 23 %, indicating the presence of a large amount of Fe<sup>2+</sup> in the original Fe-Si-B<sup>AR</sup> (Fig. 5e). After degradation, the ratio for peak Fe<sup>2+</sup> (710.2 eV) and Fe<sup>3+</sup> (711.7 eV) changed, showing that Fe<sup>2+</sup> and Fe<sup>3+</sup> played important roles during catalytic degradation process. For O 1s (Fig. 6a–6c), it was inferred that iron oxides and hydroxyl oxidize iron were formed. These results were consistent with the study of Jia et al. [58]. From the XPS results of Si 2p (Fig. 6d–6f), it can be seen that the proportion of the area for Si-Si peak to the total area of Si 2p peak decreased from 25.0 % (original Fe-Si-B<sup>AR</sup>) to 12.1 % (Fe-Si-B<sup>AR</sup> after one reuse cycle), and continuously declined to 5.7 % (Fe-Si-B<sup>AR</sup> after ten reuse cycles), while the proportion of the area for Si-O peak to the total area increased from 75.0 % (original Fe-Si-B<sup>AR</sup>) to 87.9 % (Fe-Si-B<sup>AR</sup> after one reuse cycle), and 87.9 % (Fe-Si-B<sup>AR</sup> after ten reuse cycles) which indicated that the Si atoms were oxidized to the Si oxides in the catalytic degradation process. A similar phenomenon occurred for B (Fig. 6g–6i), where the proportion of the area for B-B peak to the total area of B 1s peak decreased from 24.7 % for original Fe-Si-B<sup>AR</sup> to 0% for Fe-Si-B<sup>AR</sup> after one and ten reuse cycles. These results indicated that amorphous structured B atoms (B–B bond) in the ribbon after one and ten reuse cycles were much lower than in the original Fe-Si-B<sup>AR</sup>, and were gradually converted into B oxides (B–O bond). Compared with Fe powders, amorphous and crystallized Fe-Si-B ribbon had excellent catalytic degradation performance, which indicated that the addition of Si and B elements can improve the catalytic performance. The XRD results for original and Fe-Si-B<sup>AR</sup> after one or ten degradation reuse cycles also showed that Fe-Si-B<sup>AR</sup> kept amorphous status throughout the degradation processes (Fig. 7).

### 3.4. Catalytic degradation mechanism of Fe-Si-B<sup>AR</sup>

In order to further understand the excellent catalytic degradation performance of Fe-Si-B<sup>AR</sup>, influence of different reaction conditions, generation of reactive species, its activation energy, surface atomic activity and its adsorption ability for H<sub>2</sub>O<sub>2</sub> were conducted for mechanism study. Influence of different reaction conditions including H<sub>2</sub>O<sub>2</sub> concentration, ribbon dosage, initial concentration of 3,5-DiClSA for degradation was carried out and the results were shown in Fig. 8.

#### 3.4.1. Effect of H<sub>2</sub>O<sub>2</sub> concentration

The effect of H<sub>2</sub>O<sub>2</sub> concentration on the degradation efficiency of 3,5-DiClSA using Fe-Si-B<sup>AR</sup> was displayed in Fig. 8a. The concentration of H<sub>2</sub>O<sub>2</sub> in experimental group was set as 0, 2, 4, 6, 8 and 16 mmol L<sup>-1</sup>, while keeping other reaction conditions constant:  $T = 298 \text{ K}$ , pH = 7.0, ribbon dosage =  $4 \text{ g L}^{-1}$ , and concentration of 3,5-DiClSA =  $1.2 \mu\text{mol L}^{-1}$ . According to the degradation curve (Fig. 8a) and the histogram of reaction rate constant (Fig. 8e), the reaction rate constant firstly increased and then decreased with the increase of H<sub>2</sub>O<sub>2</sub> concentration.

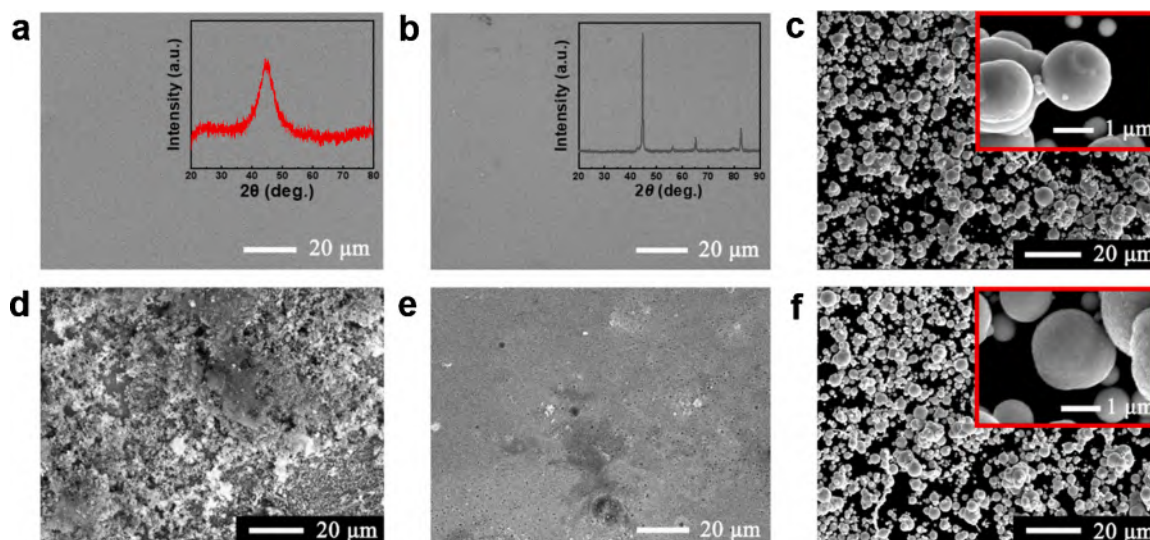


Fig. 4. SEM patterns of original (a) Fe-Si-B<sup>AR</sup> (the inset graph shows the XRD pattern), (b) Fe-Si-B<sup>CR</sup> (the inset graph shows the XRD pattern) and (c) Fe powders; SEM patterns of (d) Fe-Si-B<sup>AR</sup> after degradation (keep surface sediments), (e) Fe-Si-B<sup>CR</sup> after degradation, and (f) Fe powder after degradation.

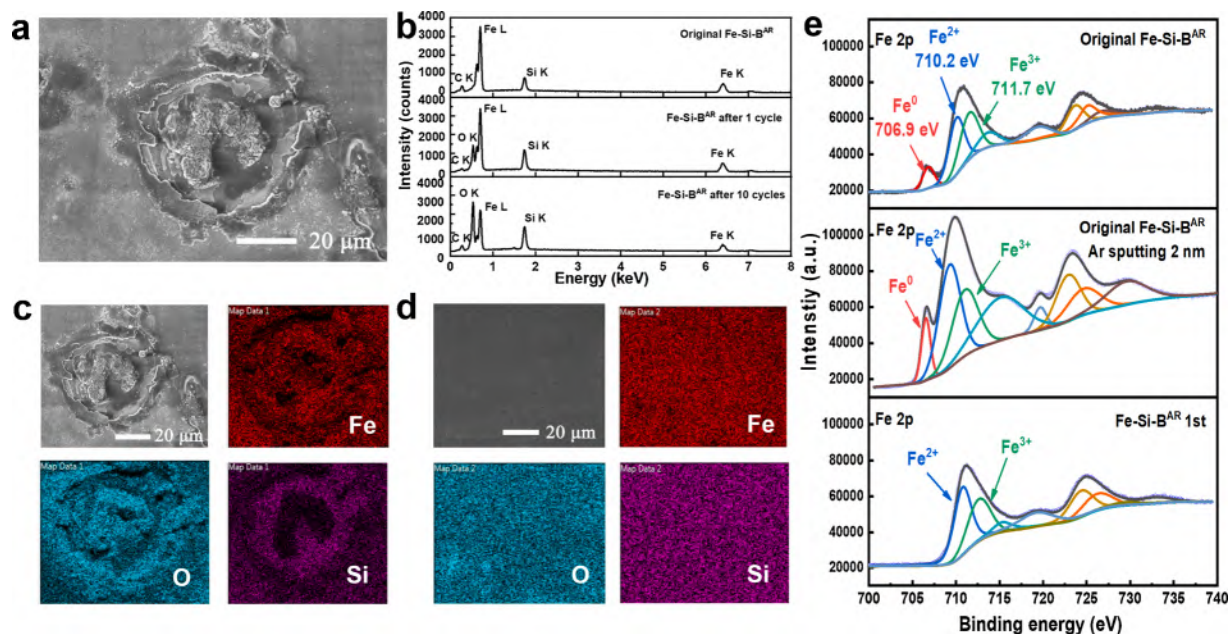


Fig. 5. (a) SEM pattern of Fe-Si-B<sup>AR</sup> after degradation (after removing of surface sediments); (b) EDS results of original Fe-Si-B<sup>AR</sup> and Fe-Si-B<sup>AR</sup> after one and ten reuse cycles; (c) EDS mapping in corrosion pit of (a); (d) EDS mapping in intact region on the surface of Fe-Si-B<sup>AR</sup> after degradation; (e) XPS spectra for Fe 2p of original Fe-Si-B<sup>AR</sup>, original Fe-Si-B<sup>AR</sup> after Ar sputting 2 nm and original Fe-Si-B<sup>AR</sup> after degradation.

**Table 1**  
EDS analysis of original Fe-Si-B<sup>AR</sup>, Fe-Si-B<sup>AR</sup> after one and ten reuse cycles.

Element	Original Fe-Si-B <sup>AR</sup> (Atom %)	Fe-Si-B <sup>AR</sup> after 1 cycle (Atom %)	Fe-Si-B <sup>AR</sup> after 10 cycles (Atom %)
Fe K	76.32	65.41	41.82
Si K	9.10	12.11	12.01
O K	–	18.56	35.33
C K	14.58	3.92	10.84

When H<sub>2</sub>O<sub>2</sub> reached 4 mmol L<sup>-1</sup>, the reaction rate constant reached maximum (0.0164 min<sup>-1</sup>).

### 3.4.2. Effect of ribbon dosage of Fe-Si-B<sup>AR</sup>

The effect of ribbon dosage of Fe-Si-B<sup>AR</sup> on the degradation efficiency of 3,5-DiClSA was shown in Fig. 8b. The ribbon dosage of Fe-Si-B<sup>AR</sup> in was set as 0, 2, 4, 6, 8 and 12 g/L, while keeping other reaction conditions constant:  $T = 298$  K,  $\text{pH} = 7.0$ ,  $C_{\text{H}_2\text{O}_2} = 4$  mmol L<sup>-1</sup>, and concentration of 3,5-DiClSA = 1.2 μmol L<sup>-1</sup>. According to the degradation curve (Fig. 8b) and the histogram of reaction rate constant (Fig. 8f), their reaction rate constants can be obtained to be 0.0049, 0.0115, 0.0158, 0.0207 and 0.0269 min<sup>-1</sup> for ribbon dosage = 2, 4, 6, 8 and 12 g L<sup>-1</sup>, respectively. These results indicated that the degradation rate of 3,5-DiClSA accelerated with the increment of ribbon dosage owing to

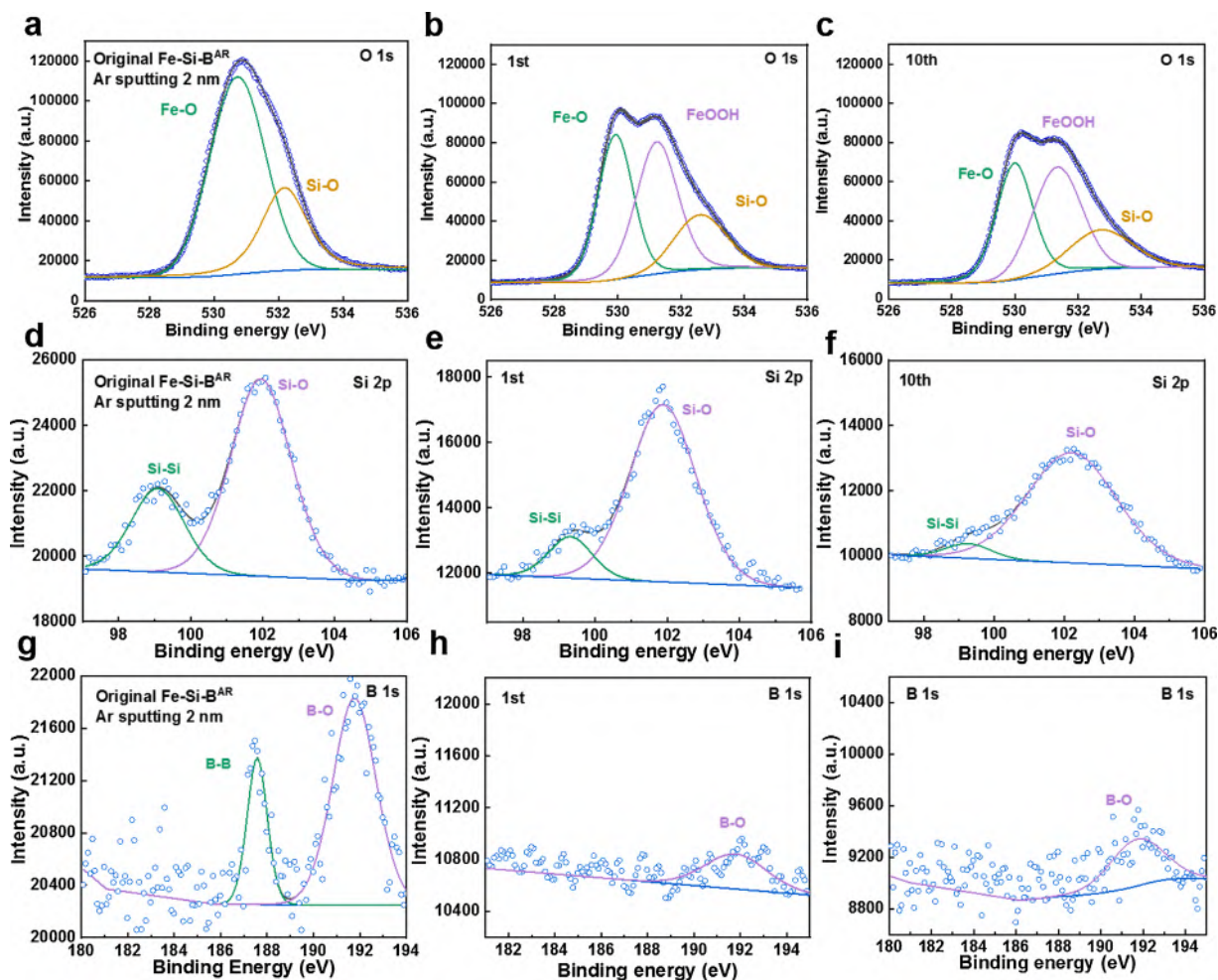


Fig. 6. High resolution XPS spectra of (a-c) O 1s, (d-f) Si 2p, and (g-i) B 1s for the original and reused Fe-Si-B<sup>AR</sup> after degradation by one or ten reuse cycles.

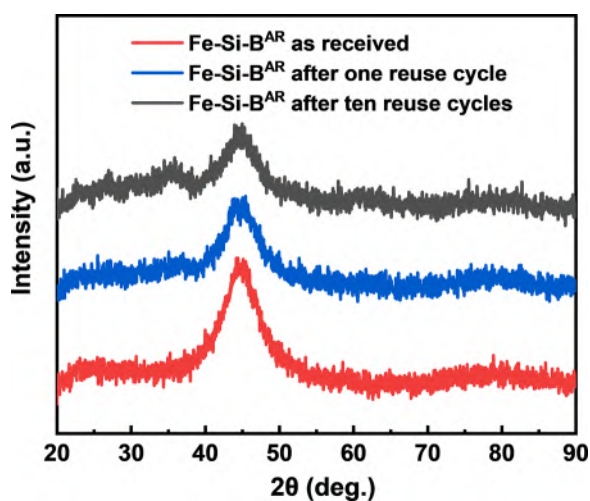


Fig. 7. XRD patterns of original and reused Fe-Si-B<sup>AR</sup> after degradation by one or ten reuse cycles.

more available reaction sites being provided.

### 3.4.3. Effect of initial concentration of 3,5-DiClSA

Effect of initial concentration of 3,5-DiClSA on its degradation efficiency using Fe-Si-B<sup>AR</sup> was displayed in Fig. 8c. Different initial concentrations of 3,5-DiClSA in experimental groups were set as 0.6, 1.2,

1.8 and 2.4  $\mu\text{mol L}^{-1}$  and other reaction conditions were kept constant:  $T = 298 \text{ K}$ ,  $\text{pH} = 7.0$ , ribbon dosage = 4  $\text{g L}^{-1}$ , and  $\text{C}_{\text{H}_2\text{O}_2} = 4 \text{ mmol L}^{-1}$ . As can be seen from Fig. 8g, their reaction rate constants can be obtained to be 0.0137, 0.0171, 0.0170 and 0.0188  $\text{min}^{-1}$  for  $\text{C}_{3,5\text{-DiClSA}} = 0.6, 1.2, 1.8$  and 2.4  $\mu\text{mol L}^{-1}$ , respectively, suggesting that available reaction sites for degradation 3,5-DiClSA were not saturated below concentration of 2.4  $\mu\text{mol L}^{-1}$ .

### 3.4.4. Generation of reactive species

To test whether reactive species such as hydroxyl radical ( $\cdot\text{OH}$ ) or  $\text{Fe}^{\text{IV}}$  was generated by the degradation system, DMPO was selected as a spin-trapping reagent for reactive species and the results are shown in Fig. 9. Compared with control group (8  $\text{mmol L}^{-1}$   $\text{H}_2\text{O}_2$ ), characteristic signals of DMPO-OH (1:2:2:1, four lines) appeared in EPR spectrums of experimental group (red line). By using a higher concentration of DMPO (30  $\text{mmol L}^{-1}$ ) compared to relatively lower concentration (10  $\text{mmol L}^{-1}$ ), more reactive species could be spin trapped as a result of higher EPR intensity (blue lines). Even after the addition of 3,5-DiClSA (1.2  $\mu\text{mol L}^{-1}$ ) to the experimental group and reacted for several minutes, signals of DMPO-OH could still be detected (blue line). As DMPO-OH adduct could be formed between  $\cdot\text{OH}$  and DMPO or being directly oxidized by  $\text{Fe}^{\text{IV}}$  [37], these results indicated that reactive species such as  $\cdot\text{OH}$  or  $\text{Fe}^{\text{IV}}$  was existed in the degradation system. To test whether the reactive species were  $\cdot\text{OH}$  or high-valent iron, isopropanol was selected as  $\cdot\text{OH}$  scavenger to prove the existence of  $\cdot\text{OH}$  in the degradation system. As can be seen from Fig. S5, the results showed that the degradation process of 3,5-DiClSA was not influenced by addition of isopropanol (6  $\text{mmol/L}$ ). Considering that isopropanol is a strong scavenger towards

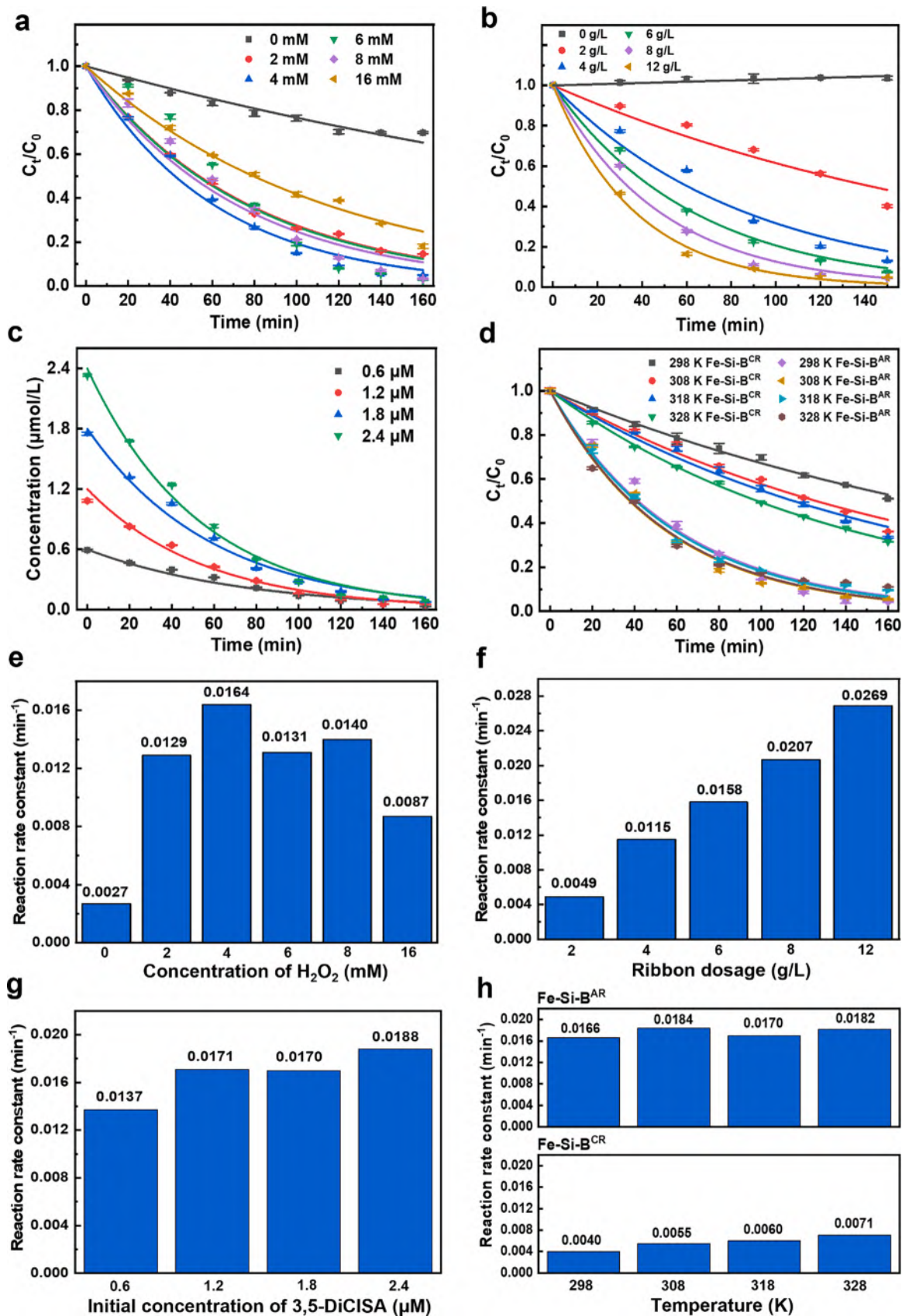


Fig. 8. Effects of different conditions (a) concentration of  $H_2O_2$ , (b) ribbon dosage, (c) initial concentration on the catalytic degradation behavior of 3,5-DiCISA by Fe-Si-B<sup>AR</sup>. (d) Effect of temperature on the catalytic degradation behavior of 3,5-DiCISA by Fe-Si-B<sup>AR</sup> and Fe-Si-B<sup>CR</sup>; (e-h) Histograms of reaction rate constants for degradation of 3,5-DiCISA by Fe-Si-B<sup>AR</sup> and Fe-Si-B<sup>CR</sup> under different conditions.

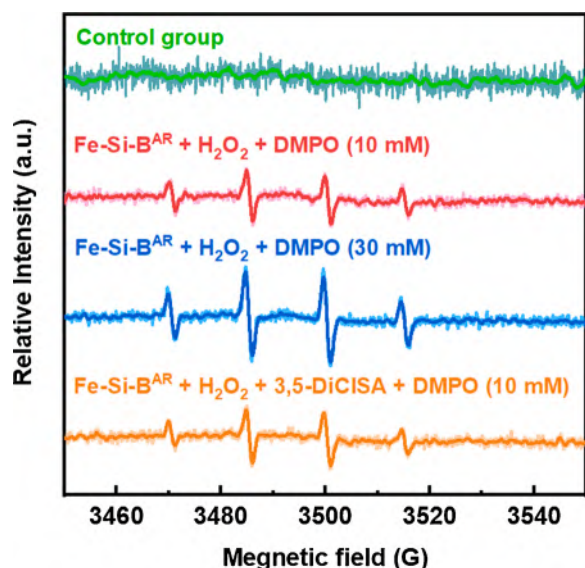


Fig. 9. EPR spectra of DMPO-OH generated from  $\text{H}_2\text{O}_2$  activation by Fe-Si-B<sup>AR</sup> (Fe-Si-B<sup>AR</sup> dosage: 4 g/L,  $\text{C}_{\text{H}_2\text{O}_2}$  = 8 mmol/L,  $\text{C}_{3,5\text{-DiClSA}}$  = 1.2  $\mu\text{mol/L}$ ).

$\cdot\text{OH}$  with a high reaction rate constant ( $k = 9.7 \times 10^8 \text{ M}^{-1} \text{ s}^{-1}$ ) [59], it was proved that  $\cdot\text{OH}$  was not existed in the degradation system in neutral condition.

Besides, methyl phenyl sulfoxide (PMSO) was also selected as a probe to see whether it can be oxidized to methyl phenyl sulfone ( $\text{PMSO}_2$ ) to prove the existence of  $\text{Fe}^{\text{IV}}$  [34–37] by using UPLC-ESI-tqMS in positive ionization mode. The product ion scan of mixed standards of PMSO (0.1 mmol/L) and  $\text{PMSO}_2$  (0.1 mmol/L) dissolved in 1/1 (v/v) acetonitrile/water were shown in Fig. S6. By applying the multiple reaction monitoring (MRM) of (141→124) for PMSO with RT of 2.85 min and (157→79) for  $\text{PMSO}_2$  with RT of 3.11 min (Fig. S7), the concentration changes of PMSO and  $\text{PMSO}_2$  can be sensitively measured. Oxidation process of PMSO in the Fe-Si-B<sup>AR</sup> based degradation system was set as: PMSO (0.1 mmol/L) in the presence of Fe-Si-B<sup>AR</sup> ribbon (4 g/L), and  $\text{H}_2\text{O}_2$  (4 mmol/L) at pH = 7.0. After PMSO was oxidized for 10 min, 450  $\mu\text{L}$  reaction solution was withdrawn, quenched with 50  $\mu\text{L}$   $\text{Na}_2\text{S}_2\text{O}_3$  (0.1 mol/L), and analyzed by UPLC-ESI-tqMS for PMSO and  $\text{PMSO}_2$ . Interestingly, after reaction for 10 min, generation of  $\text{PMSO}_2$  (RT = 3.09 min), which corresponding to the standard peak of  $\text{PMSO}_2$  (RT = 3.11 min) can be found in the Fe-Si-B<sup>AR</sup> based degradation system under neutral condition, accompanying with slight decrease of PMSO (RT = 2.85 min), indicating that  $\text{Fe}^{\text{IV}}$  rather than  $\cdot\text{OH}$  was formed which accounted for degradation of 3,5-DiClSA (Fig. 10). The transformation rate of PMSO to  $\text{PMSO}_2$  was relatively low because  $\text{Fe}^{\text{IV}}$  reacted sluggishly with PMSO at pH = 7.0 with a reported rate constant of lower than  $1.5 \times 10^{-2} \text{ M}^{-1} \text{ s}^{-1}$  [36]. These results were in accordance with recent study from Wang et al. (2020) [34] and Huang et al. (2021) [36], which also supported the idea that  $\text{Fe}^{\text{IV}}$  is capable of allowing selective oxidation. As far as we know, this is the first time that the generation of  $\text{Fe}^{\text{IV}}$  by using Fe-Si-B amorphous catalyst has been proved by using PMSO as the probe.

### 3.4.5. Activation energy

Degradations of 3,5-DiClSA at  $T = 298 \text{ K}$ , 308 K, 318 K and 328 K using Fe-Si-B<sup>AR</sup> and Fe-Si-B<sup>CR</sup> were performed to analyze and compare their activation energy difference, the reaction conditions were: ribbon dosage = 4 g  $\text{L}^{-1}$ , pH = 7.0,  $\text{C}_{3,5\text{-DiClSA}}$  = 1.2  $\mu\text{mol L}^{-1}$ , and  $\text{C}_{\text{H}_2\text{O}_2}$  = 4 mmol  $\text{L}^{-1}$ . Normalized concentration changes of degradation processes using Fe-Si-B<sup>AR</sup> and Fe-Si-B<sup>CR</sup> at different temperatures and their fitting curves are shown in Fig. 8d. Reaction rate constants can be measured and calculated as 0.0166  $\text{min}^{-1}$ , 0.0184  $\text{min}^{-1}$ , 0.0170  $\text{min}^{-1}$  and 0.0182  $\text{min}^{-1}$  for Fe-Si-B<sup>AR</sup> and 0.0040  $\text{min}^{-1}$ , 0.0055  $\text{min}^{-1}$ ,

0.0060  $\text{min}^{-1}$ , 0.0071  $\text{min}^{-1}$  for Fe-Si-B<sup>CR</sup> at 298 K, 308 K, 318 K and 328 K (Fig. 8h), respectively, according to their fitting results. The activation energy of the reaction can be obtained according to Arrhenius equation:

$$\ln k_T = -E_a/RT + \ln A \quad (2)$$

where  $k_T$ ,  $E_a$ ,  $R$ ,  $T$  and  $A$  represent reaction rate constant at different temperature, the activation energy, the gas constant, temperature and a constant, respectively. The results of  $\ln k_T$  vs.  $-1/RT$  were plotted in Fig. 11a and fitted linearly. The slope of the fitted line was the activation energy. The activation energy of Fe-Si-B<sup>AR</sup> and Fe-Si-B<sup>CR</sup> in this degradation process was obtained to be 1.62  $\text{kJ mol}^{-1}$  and 14.76  $\text{kJ mol}^{-1}$ , respectively. Activation energy of the former was approximately only 1/9 of the latter. The lower activation energy made the degradation reaction easier to undertake, which also explains why the catalytic degradation rate of 3,5-DiClSA by Fe-Si-B<sup>AR</sup> was faster than by Fe-Si-B<sup>CR</sup>.

### 3.4.6. Surface atomic activity and adsorption ability for $\text{H}_2\text{O}_2$

The excellent catalytic degradation of Fe-Si-B<sup>AR</sup> can be ascribed to its fast surface mobility owing to the unique amorphous structures. Researchers have suggested that the surface diffusion rate of amorphous alloy was much higher than its crystalline counterpart [14,60–62], which indicated that there was an active "liquid like" layer on the surface of amorphous alloy. The dynamic modulus mapping (DMM, in Fig. 11b) of Fe-Si-B<sup>AR</sup> and Fe-Si-B<sup>CR</sup> was conducted, and the modulus distribution histograms (Fig. 11c) indicated that the former had lower modulus distribution on its surface than the latter. This means Fe-Si-B<sup>AR</sup> had active kinetic behavior, showing an active "liquid like" layer on Fe-Si-B<sup>AR</sup>.  $\text{Fe}^{2+}$  in the active "liquid like" layer had excellent reactivity and was easy to be oxidized by  $\text{H}_2\text{O}_2$ , leading to the production of  $\text{Fe}^{\text{IV}}$ . Thus, it's speculated that the three materials Fe-Si-B<sup>AR</sup>, Fe-Si-B<sup>CR</sup>, and Fe powder had different ability to adsorb  $\text{H}_2\text{O}_2$ , which resulted in different efficiencies in  $\text{Fe}^{\text{IV}}$  production. To verify this, the adsorption energies ( $E_{\text{ads}}$ ) for three materials Fe-Si-B<sup>AR</sup>, Fe-Si-B<sup>CR</sup>, and Fe powder towards  $\text{H}_2\text{O}_2$  were calculated by using density functional theory (DFT) method and the results are shown in Fig. 11d. It is noted that  $E_{\text{ads}}$  followed the order of  $\text{Fe-Si-B}^{\text{AR}} < \text{Fe-Si-B}^{\text{CR}} < \text{Fe powder}$ , among which Fe-Si-B<sup>AR</sup> had more negative  $E_{\text{ads}}$  than others, indicating that the unique structure of Fe-Si-B<sup>AR</sup> made itself easier to adsorb  $\text{H}_2\text{O}_2$  than other two materials, and more adsorptions of  $\text{H}_2\text{O}_2$  were conducive to the reaction between  $\text{Fe}^{2+}$  and  $\text{H}_2\text{O}_2$  to produce  $\text{Fe}^{\text{IV}}$ , which facilitated the Fenton-like reaction and accelerated the degradation process.

Based on the above discussion, pretty low activation energy of Fe-Si-B<sup>AR</sup> (only 1/9 of that of Fe-Si-B<sup>CR</sup>), active  $\text{Fe}^{2+}$  in active "liquid like" layer and stronger adsorption ability for  $\text{H}_2\text{O}_2$  endowed Fe-Si-B<sup>AR</sup> with better catalytic degradation performance for 3,5-DiClSA. Combined with the fact that the ratio of  $\text{Fe}^{2+}$  and  $\text{Fe}^{3+}$  changed during the degradation process and the generation of  $\text{Fe}^{\text{IV}}$ , it is reasonable to suggest a mechanism of catalytic degradation of 3,5-DiClSA using Fe-Si-B ribbons by Fenton-like reaction (Fig. 11e). The process can be described as the following steps:



Oxidation of  $\text{Fe}^{2+}$  by  $\text{H}_2\text{O}_2$  produced  $\text{Fe}^{\text{IV}}$  under neutral condition, which accounted for the degradation of 3,5DiClSA. The  $\text{Fe}^{\text{IV}}$  could be further oxidized by  $\text{H}_2\text{O}_2$ , and produced  $\text{Fe}^{2+}$ . After  $\text{H}_2\text{O}_2$  was consumed in the degradation system,  $\text{Fe}^{\text{IV}}$  could reacted with  $\text{H}_2\text{O}$  to produce  $\text{Fe}^{3+}$ . Thus, the reaction between  $\text{Fe}^{2+}$  and  $\text{H}_2\text{O}_2$  is important for the degradation of the pollutant.  $\text{Fe}^{2+}$  in Fe-Si-B<sup>AR</sup> was easier to be oxidized by  $\text{H}_2\text{O}_2$  than crystalline counterpart for the above-mentioned reasons. Adsorption of  $\text{H}_2\text{O}_2$  onto the ribbon surface could be crucial for the catalytic reaction.

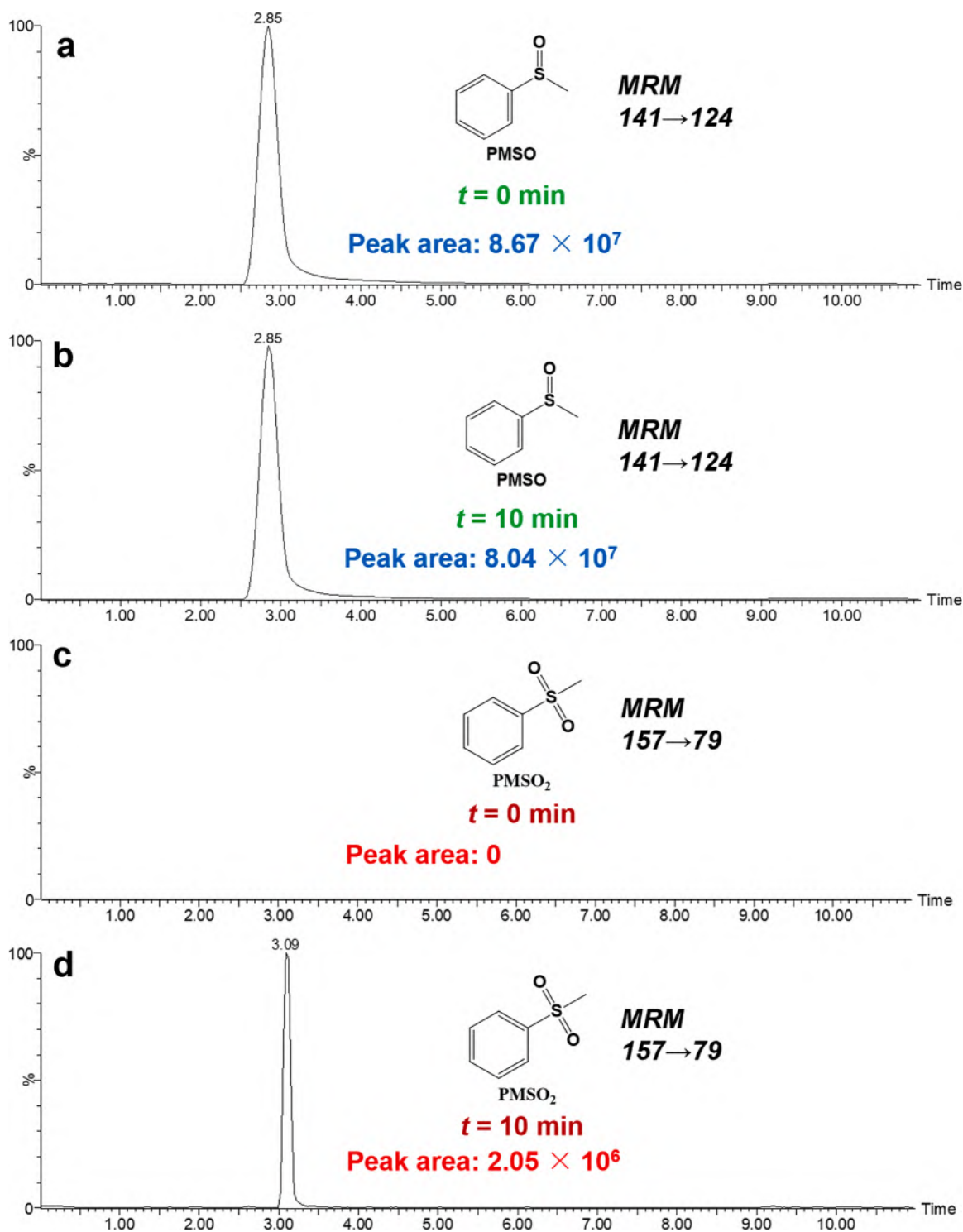


**Fig. 10.** UPLC/ESI-tqMS MRM spectra of oxidation process of PMSO (141→124) and formation of PMSO<sub>2</sub> (157→79) by Fe-Si-B<sup>AR</sup> based degradation system: (a) MRM spectra of PMSO at  $t = 0$  min; (b) MRM spectra of PMSO at  $t = 10$  min; (c) MRM spectra of PMSO<sub>2</sub> at  $t = 0$  min; (d) MRM spectra of PMSO<sub>2</sub> at  $t = 10$  min (Ribbon dosage =  $4 \text{ g L}^{-1}$ , pH = 7.0,  $C_{\text{H}_2\text{O}_2} = 4 \text{ mmol L}^{-1}$ ,  $C_{\text{PMSO}} = 0.1 \text{ mmol L}^{-1}$ ).

### 3.5. Reusability and renewable catalytic degradation performance

Reusability is a key parameter for catalysis in terms of practical application. Here, reusability of Fe-Si-B<sup>AR</sup> in degradation of 3,5-DiClSA ranging from one to ten reuse cycles under neutral condition was investigated. After each degradation cycle, the ribbons after degradation process were removed of sediments on the surface by ultrasonic cleaning and rinsed well with ultrapure water. The reaction conditions were set as

follows:  $T = 298 \text{ K}$ , pH = 7.0, ribbon dosage =  $8 \text{ g L}^{-1}$ ,  $C_{3,5\text{-DiClSA}} = 1.2 \text{ } \mu\text{mol L}^{-1}$ ,  $C_{\text{H}_2\text{O}_2} = 4 \text{ mmol L}^{-1}$ , and the results were shown in Fig. 12a. It can be seen that the degradation efficiency of 3,5-DiClSA reached 95 % in 120 min in each of ten degradation cycles. In terms of reaction rate, the overall trend of reaction rate increased with reused cycles (Fig. 12b). It's worth noting that the reaction rate constant in the 10th degradation cycle by Fe-Si-B<sup>AR</sup> ( $0.0453 \text{ min}^{-1}$ ) was more than twice of that in the 1st degradation cycle ( $0.0224 \text{ min}^{-1}$ ). Thus, Fe-Si-

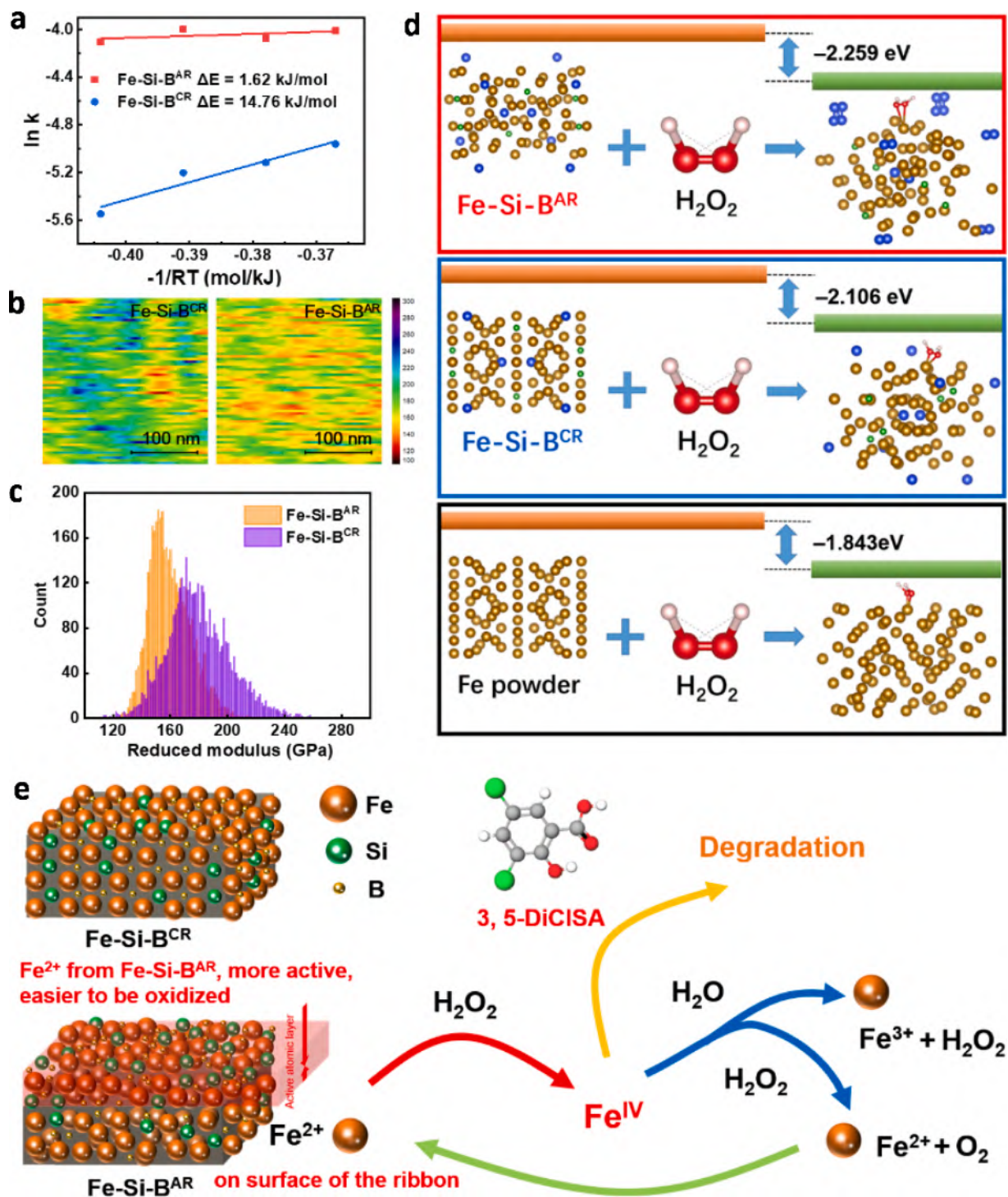


**Fig. 11.** Mechanism study for excellent catalytic degradation performance of Fe-Si-B<sup>AR</sup>. (a) The Arrhenius plot for degradation process of 3,5-DiCISA by Fe-Si-B<sup>AR</sup> and Fe-Si-B<sup>CR</sup> (Ribbon dosage = 4 g L<sup>-1</sup>, pH = 7.0, C<sub>3,5-DiCISA</sub> = 1.2 μmol L<sup>-1</sup>, C<sub>H<sub>2</sub>O<sub>2</sub></sub> = 4 mmol L<sup>-1</sup>); (b) Dynamic modulus mapping of Fe-Si-B<sup>AR</sup> and Fe-Si-B<sup>CR</sup>; (c) Modulus distribution histogram of two materials; (d) DFT calculation results; (e) Mechanism of catalytic degradation for 3,5-DiCISA by Fe-Si-B<sup>AR</sup> and Fe-Si-B<sup>CR</sup>.

B<sup>AR</sup> was not only durable but showed better and better catalytic degradation performance in reuse processes when applied in degradation of 3,5-DiCISA under neutral condition.

The surface morphologies of the Fe-Si-B<sup>AR</sup> after one and ten degradation cycles were also compared. After 1st degradation cycle, a pit shaped reaction area appeared on the surface of Fe-Si-B<sup>AR</sup>, but the surrounding pit remained complete with only a few cracks (Fig. 12c). The surface of Fe-Si-B<sup>AR</sup> after 10 degradation cycles was broken like a cracked land (Fig. 12d), and the old fragile surface peeled off, revealing

"fresh" rough pits below. These fresh pits were more active than the exfoliated area, and the cracks and pits would continuously form during the catalytic reaction process, which provided more active sites. These phenomena were in accordance with study from Wang et al. [63], that the FePC amorphous ribbon had self-renewing behavior for highly efficient decolorization of methylene blue. After several cycles, most of Fe<sup>2+</sup> on the ribbon surface were consumed and then the fragile layer peeled off, exposing the deep and fresh surface, which renewed the catalytic performance of the ribbon.

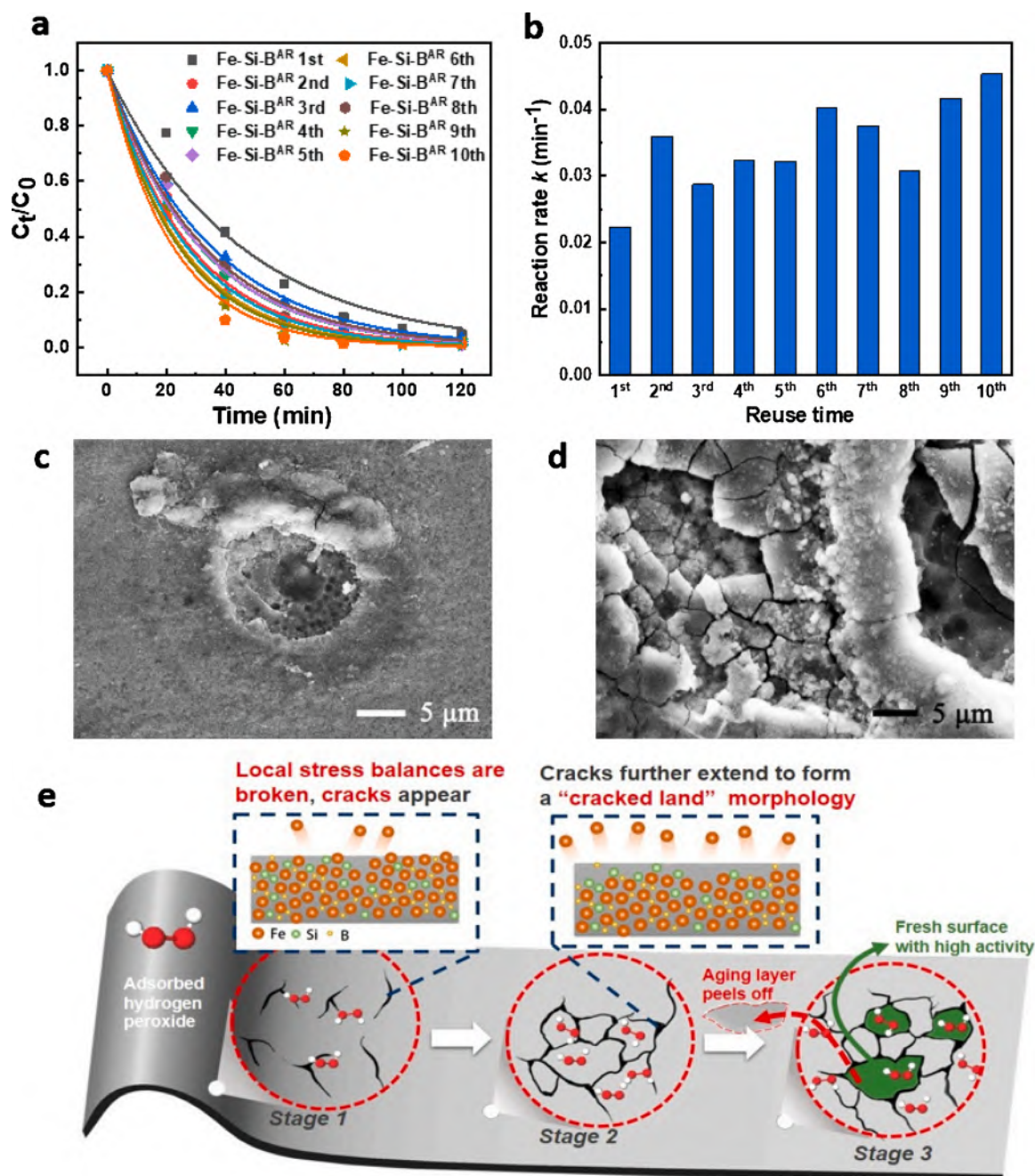


**Fig. 12.** Durability study for catalytic degradation performance of Fe-Si-B<sup>AR</sup>. (a) Catalytic degradation behavior of Fe-Si-B<sup>AR</sup> used in degradation of 3,5-DiClSA from 1st to 10th cycle ( $T = 298$  K,  $\text{pH} = 7.0$ , ribbon dosage =  $8 \text{ g L}^{-1}$ ,  $C_{3,5\text{-DiClSA}} = 1.2 \mu\text{mol L}^{-1}$ ,  $C_{\text{H}_2\text{O}_2} = 4 \text{ mmol L}^{-1}$ ); (b) Reaction rate constants for each reuse cycle by Fe-Si-B<sup>AR</sup>; SEM micrographs of ribbons after (c) one, and (d) ten reuse cycles; (e) Schematic diagram of excellent durability mechanism of Fe-Si-B<sup>AR</sup>.

From the above analysis, it's reasonable to propose a mechanism to explain the excellent durability and "better and better" catalytic degradation performance of Fe-Si-B<sup>AR</sup>, as shown in the Fig. 12e. It is well known that the internal stress distribution of amorphous alloy is very uneven compared with their crystallized counterpart [57,64,65]. Based on the EDS results above (Fe:Si changed from 8.38 for original Fe-Si-B<sup>AR</sup> to 3.48 for Fe-Si-B<sup>AR</sup> after ten reuse cycles), a large amount of Fe<sup>2+</sup> were detached from Fe-Si-B<sup>AR</sup> surface in the catalytic degradation process, which broke local stress balance and cracks were formed. As more and more Fe<sup>2+</sup> detached, the cracks extended to form the morphology similar to the cracked land. Then the old fragile surfaces would break away, exposing the fresh pits in deep surface. On one hand, these fresh surfaces were more active than those detached surfaces, which was equivalent to self-renewing Fe-Si-B<sup>AR</sup>. On the other hand, the increasing

cracks and rough pits increased the active sites for reaction, making the reaction faster.

#### 4. Conclusions

In summary, the catalytic degradation performances of Fe-Si-B<sup>AR</sup>, Fe-Si-B<sup>CR</sup> and Fe powder in degradation of 3,5-DiClSA under neutral condition were compared. The degradation rate by Fe-Si-B<sup>AR</sup> was faster than by Fe-Si-B<sup>CR</sup>, while degradation by Fe powder almost did not occur. The reaction rate constant of Fe-Si-B<sup>AR</sup> was  $0.0166 \text{ min}^{-1}$ , which was more than four times as high as that of Fe-Si-B<sup>CR</sup> ( $0.0040 \text{ min}^{-1}$ ). High-valent iron of Fe<sup>IV</sup> could be generated which accounted for degradation of 3,5-DiClSA. The characteristics of lower activation energy, faster surface mobility and higher adsorption ability towards H<sub>2</sub>O<sub>2</sub> for Fe-Si-B<sup>AR</sup> were

the main reasons that accounted for its highest catalytic degradation efficiency towards 3,5-DiCISA among three materials. The durability test of Fe-Si-B<sup>AR</sup> also showed that the catalytic degradation performance of Fe-Si-B<sup>AR</sup> became better and better with rate constant increased from 0.0224 min<sup>-1</sup> (1st degradation) to 0.0453 min<sup>-1</sup> (10th degradation) during 10 degradation cycles under neutral condition. The present study showed that Fe-Si-B<sup>AR</sup> could potentially become a promising catalyst for the degradation of 3,5-DiCISA or other DBPs by Fenton-like reaction without adjusting pH in control of DBPs in drinking water. The application of other type of AOPs such as sulfate radical based AOPs, which could also be activated by Fe-based catalyst, in water treatment process worth further investigation.

#### CRedit authorship contribution statement

**Libo Zhang:** Formal analysis, Investigation, Writing - original draft. **Lianxiang Qiu:** Formal analysis, Investigation. **Qingyao Zhu:** Formal analysis, Investigation. **Xiong Liang:** Conceptualization, Writing - review & editing. **Jingxiang Huang:** Investigation. **Mengting Yang:** Conceptualization, Formal analysis. **Zhenxuan Zhang:** Conceptualization, Methodology, Software, Supervision, Writing - review & editing. **Jiang Ma:** Conceptualization, Supervision, Funding acquisition, Writing - review & editing. **Jun Shen:** Resources.

#### Declaration of Competing Interest

The authors declare that they have no known competing financial interests or personal relationships that could have appeared to influence the work reported in this paper.

#### Acknowledgements

The work was supported by the Key Basic and Applied Research Program of Guangdong Province, China (Grant No. 2019B030302010), the National Natural Science Foundation of China (Grant No. 51871157, 51971150), the Science and Technology Innovation Commission of Shenzhen (Grants No. JCYJ20170412111216258), the National Key Research and Development Program of China (Grant No. 2018YFA0703605). The authors thank the assistance on microscope observation received from the Electron Microscope Center of the Shenzhen University. We would also like to express our thanks to Junyi Wang from Southern University of Science and Technology for her assistance in EPR testing.

#### Appendix A. Supplementary data

Supplementary material related to this article can be found, in the online version, at <https://doi.org/10.1016/j.apcatb.2021.120258>.

#### References

- [1] S.D. Richardson, Disinfection by-products and other emerging contaminants in drinking water, *TrAC, Trends Anal. Chem.* 22 (2003) 666–684.
- [2] M.T. Yang, X.R. Zhang, Q.H. Liang, B. Yang, Application of (LC/MS/MS precursor ion scan for evaluating the occurrence, formation and control of polar halogenated DBPs in disinfected waters: a review, *Water Res.* 158 (2019) 322–337.
- [3] W.D. King, L.D. Marrett, C.G. Woolcott, Case-control study of colon and rectal cancers and chlorination by-products in treated water, *Cancer Epidemiol. Biomarkers Prev.* 9 (2000) 813–818.
- [4] A.H. Zhang, F.F. Wang, W.H. Chu, X. Yang, Y. Pan, H.F. Zhu, Integrated control of CX<sub>3</sub>R-type DBP formation by coupling thermally activated persulfate pre-oxidation and chloramination, *Water Res.* 160 (2019) 304–312.
- [5] N. Chaukura, S.S. Marais, W. Moyo, N. Mbali, L.C. Thakalekoala, T. Ingwani, B. B. Mamba, P. Jarvis, T.T.I. Nkambule, Contemporary issues on the occurrence and removal of disinfection byproducts in drinking water—a review, *J. Environ. Chem. Eng.* 8 (2020) 103659.
- [6] J.L. Sun, D.Z. Kong, E. Aghdam, J.Y. Fang, Q.Y. Wu, J.J. Liu, Y. Du, X. Yang, C. Shang, The influence of the UV/chlorine advanced oxidation of natural organic matter for micropollutant degradation on the formation of DBPs and toxicity during post-chlorination, *Chem. Eng. J.* 373 (2019) 870–879.
- [7] S. Chen, W. Chu, H. Wei, H. Zhao, B. Xu, N. Gao, D. Yin, Reductive dechlorination of haloacetamides in drinking water by Cu/Fe bimetal, *Sep. Purif. Technol.* 203 (2018) 226–232.
- [8] C. Liu, D.W. Chen, Y.Y. Ren, W. Chen, Removal efficiency and mechanism of phycocyanin in water by zero-valent iron, *Chemosphere* 218 (2019) 402–411.
- [9] Q.F. Wang, Y.S. Shao, N.Y. Gao, S.S. Liu, L. Dong, P.H. Rao, W.H. Chu, B. Xu, N. An, J. Deng, Impact of zero valent iron/persulfate preoxidation on disinfection byproducts through chlorination of alachlor, *Chem. Eng. J.* 380 (2020) 122435.
- [10] Y.K. Sun, J.X. Li, T.L. Huang, X.H. Guan, The influences of iron characteristics, operating conditions and solution chemistry on contaminants removal by zero-valent iron: a review, *Water Res.* 100 (2016) 277–295.
- [11] X. Guan, Y. Sun, H. Qin, J. Li, I.M.C. Lo, D. He, H. Dong, The limitations of applying zero-valent iron technology in contaminants sequestration and the corresponding countermeasures: the development in zero-valent iron technology in the last two decades (1994–2014), *Water Res.* 75 (2015) 224–248.
- [12] W.H. Wang, Bulk metallic glasses with functional physical properties, *Adv. Mater.* 21 (2009) 4524–4544.
- [13] Z. Li, Z. Huang, F. Sun, X. Li, J. Ma, Forming of metallic glasses: mechanisms and processes, *Mater. Today Adv.* 7 (2020) 100077.
- [14] J. Ma, C. Yang, X.D. Liu, B.S. Shang, Q.F. He, F.C. Li, T.Y. Wang, D. Wei, X. Liang, X.Y. Wu, Fast surface dynamics enabled cold joining of metallic glasses, *Sci. Adv.* 5 (2019) eaax7256.
- [15] L.C. Zhang, S.X. Liang, Fe-based metallic glasses in functional catalytic applications, *Chem. Asian J.* 13 (2018) 3575–3592.
- [16] Z.K. Li, X.D. Qin, Z.W. Zhu, S.J. Zheng, H.L. Li, H.M. Fu, H.F. Zhang, Cu-based metallic glass with robust activity and sustainability for wastewater treatment, *J. Mater. Chem. A* 8 (2020) 10855–10864.
- [17] X.Q. Wu, F.Y. Chen, N. Zhang, A. Qaseem, R.L. Johnston, A silver–copper metallic glass electrocatalyst with high activity and stability comparable to Pt/C for zinc–air batteries, *J. Mater. Chem. A* 4 (2016) 3527–3537.
- [18] J. Zhang, Y.H. Ling, W.B. Gao, S. Wang, J.T. Li, Enhanced photoelectrochemical water splitting on novel nanoflake WO<sub>3</sub> electrodes by dealloying of amorphous Fe–W alloys, *J. Mater. Chem. A* 1 (2013) 10677–10685.
- [19] L.C. Zhang, Z. Jia, F.C. Lyu, S.X. Liang, J. Lu, A review of catalytic performance of metallic glasses in wastewater treatment: recent progress and prospects, *Prog. Mater. Sci.* 105 (2019) 100576.
- [20] Y.Q. Yan, X. Liang, J. Ma, J. Shen, Rapid removal of copper from wastewater by Fe-based amorphous alloy, *Intermetallics* 124 (2020) 106849.
- [21] C.Q. Zhang, Z.W. Zhu, H.F. Zhang, Z.Q. Hu, On the decolorization property of Fe–Mo–Si–B alloys with different structures, *J. Non-Cryst. Solids* 358 (2012) 61–64.
- [22] S.X. Liang, W.C. Zhang, W.M. Wang, G.H. Jia, W.M. Yang, L.C. Zhang, Surface reactivation of FeNiPC metallic glass: A strategy for highly enhanced catalytic behavior, *J. Phys. Chem. Solids* 132 (2019) 89–98.
- [23] L. Hou, Q. Wang, X. Fan, F. Miao, W. Yang, B. Shen, Effect of Co addition on catalytic activity of FePCCu amorphous alloy for methylene blue degradation, *New J. Chem.* 43 (2019) 6126–6135.
- [24] Z. Jia, J. Kang, W.C. Zhang, W.M. Wang, C. Yang, H. Sun, D. Habibi, L.C. Zhang, Surface aging behaviour of Fe-based amorphous alloys as catalysts during heterogeneous photo-Fenton-like process for water treatment, *Appl. Catal. B* 204 (2017) 537–547.
- [25] S.X. Liang, Z. Jia, W.C. Zhang, W.M. Wang, L.C. Zhang, Rapid malachite green degradation using Fe<sub>73</sub>Si<sub>13</sub>B<sub>5</sub>Cu<sub>1</sub>Nb<sub>3</sub> metallic glass for activation of persulfate under UV-Vis light, *Mater. Des.* 119 (2017) 244–253.
- [26] F. Miao, Q.Q. Wang, Q.S. Zeng, L. Hou, T. Liang, Z.Q. Cui, B.L. Shen, Excellent reusability of FeBC amorphous ribbons induced by progressive formation of through-pore structure during acid orange 7 degradation, *J. Mater. Sci. Technol.* 38 (2020) 107–118.
- [27] X.D. Qin, Z.W. Zhu, G. Liu, H.M. Fu, H.W. Zhang, A.M. Wang, H. Li, H.F. Zhang, Ultrafast degradation of azo dyes catalyzed by cobalt-based metallic glass, *Sci. Rep.* 5 (2015) 18226.
- [28] Y. Tang, Y. Shao, N. Chen, X. Liu, S.Q. Chen, K.F. Yao, Insight into the high reactivity of commercial Fe-Si-B amorphous zero-valent iron in degrading azo dye solutions, *RSC Adv.* 5 (2015) 34032–34039.
- [29] Y. Tang, Y. Shao, N. Chen, K.F. Yao, Rapid decomposition of Direct Blue 6 in neutral solution by Fe-B amorphous alloys, *RSC Adv.* 5 (2015) 6215–6221.
- [30] J.Q. Wang, Y.H. Liu, M.W. Chen, G.Q. Xie, D.V. Louzguine-Luzgin, A. Inoue, J. H. Perepezko, Rapid degradation of azo dye by Fe-based metallic glass powder, *Adv. Funct. Mater.* 22 (2012) 2567–2570.
- [31] J.Q. Wang, Y.H. Liu, M.W. Chen, D.V. Louzguine-Luzgin, A. Inoue, J.H. Perepezko, Excellent capability in degrading azo dyes by MgZn-based metallic glass powders, *Sci. Rep.* 2 (2012) 1–6.
- [32] P.P. Wang, J.Q. Wang, J.T. Huo, W. Xu, X.M. Wang, G. Wang, Fast degradation of azo dye by nanocrystallized Fe-based alloys, *Sci. China: Phys., Mech. Astron.* 60 (2017) 076112.
- [33] P.P. Wang, J.Q. Wang, H. Li, H. Yang, J.T. Huo, J.G. Wang, C.T. Chang, X.M. Wang, R.W. Li, G. Wang, Fast decolorization of azo dyes in both alkaline and acidic solutions by Al-based metallic glasses, *J. Alloys. Compd.* 701 (2017) 759–767.
- [34] Z. Wang, W. Qiu, S. Pang, Y. Gao, Y. Zhou, Y. Cao, J. Jiang, Relative contribution of ferryl ion species (Fe(IV)) and sulfate radical formed in nanoscale zero valent iron activated peroxydisulfate and peroxymonosulfate processes, *Water Res.* 172 (2020) 115504.
- [35] H.H. Kim, H. Lee, D. Lee, Y.J. Ko, H. Woo, J. Lee, C. Lee, A.L.T. Pham, Activation of hydrogen peroxide by a titanium oxide-supported iron catalyst: evidence for surface Fe(IV) and its selectivity, *Environ. Sci. Technol.* 54 (2020) 15424–15432.
- [36] Z.S. Huang, L. Wang, Y.L. Liu, H.Y. Zhang, X.N. Zhao, J. Ma, Ferrate self-decomposition in water is also a self-activation process: role of Fe(V) species and

- enhancement with Fe(III) in methyl phenyl sulfoxide oxidation by excess ferrate, *Water Res.* 197 (2021) 117094.
- [37] L. Pan, W. Shi, T. Sen, L. Wang, J. Zhang, Visible light-driven selective organic degradation by FeTiO<sub>3</sub>/persulfate system: the formation and effect of high valent Fe(IV), *Appl. Catal. B* 280 (2021) 119414.
- [38] H. Dong, Y. Li, S. Wang, W. Liu, G. Zhou, Y. Xie, X. Guan, Both Fe(IV) and radicals are active oxidants in the Fe(II)/Peroxydisulfate process, *Environ. Sci. Technol. Lett.* 7 (2020) 219–224.
- [39] S. Liang, L. Zhu, J. Hua, W. Duan, P.T. Yang, S.L. Wang, C. Wei, C. Liu, C. Feng, Fe<sup>2+</sup>/HClO reaction produces Fe<sup>IV</sup>O<sup>2+</sup>: an enhanced advanced oxidation process, *Environ. Sci. Technol.* 54 (2020) 6406–6414.
- [40] J.Q. Liu, X.R. Zhang, Comparative toxicity of new halophenolic DBPs in chlorinated saline wastewater effluents against a marine alga: halophenolic DBPs are generally more toxic than haloaliphatic ones, *Water Res.* 65 (2014) 64–72.
- [41] Y. Pan, Y. Wang, A.M. Li, B. Xu, Q.M. Xian, C.D. Shuang, P. Shi, Q. Zhou, Detection, formation and occurrence of 13 new polar phenolic chlorinated and brominated disinfection byproducts in drinking water, *Water Res.* 112 (2017) 129–136.
- [42] Z.X. Zhang, Q.Y. Zhu, C. Huang, M.T. Yang, J.Y. Li, Y.T. Chen, B. Yang, X. Zhao, Comparative cytotoxicity of halogenated aromatic DBPs and implications of the corresponding developed QSAR model to toxicity mechanisms of those DBPs: binding interactions between aromatic DBPs and catalase play an important role, *Water Res.* 170 (2020) 115283.
- [43] Y. Zhang, Z. Lu, Z. Zhang, B. Shi, C. Hu, L. Lyu, P. Zuo, J. Metz, H. Wang, Heterogeneous Fenton-like reaction followed by GAC filtration improved removal efficiency of NOM and DBPs without adjusting pH, *Sep. Purif. Technol.* 260 (2021) 118234.
- [44] A. Samokhvalov, Analysis of various solid samples by synchronous fluorescence spectroscopy and related methods: a review, *Talanta* 216 (2020) 120944.
- [45] L. Wang, Y. Chen, B. Chen, J. Yang, Generation of hydroxyl radicals during photodegradation of chloroacetic acids by 254 nm ultraviolet: a special degradation process revealed by a holistic radical determination methodology, *J. Hazard. Mater.* 404 (2021) 124040.
- [46] S. Dong, T.H. Nguyen, M.J. Plewa, Comparative mammalian cell cytotoxicity of wastewater with elevated bromide and iodide after chlorination, chloramination, or ozonation, *J. Environ. Sci.* 58 (2017) 296–301.
- [47] G. Kresse, J. Hafner, Ab initio molecular-dynamics for liquid-metals, *Phys. Rev. B* 47 (1993) 558–561.
- [48] J. Iniguez, D. Vanderbilt, L. Bellaiche, First-principles study of (BiScO<sub>3</sub>)<sub>1-x</sub>(PbTiO<sub>3</sub>)<sub>x</sub> piezoelectric alloys, *Phys. Rev. B* 67 (2003) 224107.
- [49] R. Asahi, W. Mannstadt, A.J. Freeman, Optical properties and electronic structures of semiconductors with screened-exchange LDA, *Phys. Rev. B* 59 (1999) 7486.
- [50] B. Hammer, L.B. Hansen, J.K. Nørskov, Improved adsorption energetics within density-functional theory using revised Perdew-Burke-Ernzerhof functionals, *Phys. Rev. B* 59 (1999) 7413.
- [51] J.P. Perdew, K. Burke, M. Ernzerhof, Generalized gradient approximation made simple, *Phys. Rev. Lett.* 77 (1996) 3865.
- [52] J.P. Perdew, A. Ruzsinszky, G.I. Csonka, O.A. Vydrov, G.E. Scuseria, L. A. Constantin, X.L. Zhou, K. Burke, Restoring the density-gradient expansion for exchange in solids and surfaces, *Phys. Rev. Lett.* 100 (2008) 136406.
- [53] G.I. Csonka, J.P. Perdew, A. Ruzsinszky, P.H.T. Philipsen, S. Lebègue, J. Paier, O. A. Vydrov, J.G. Ángyán, Assessing the performance of recent density functionals for bulk solids, *Phys. Rev. B* 79 (2009) 155107.
- [54] P.E. Blöchl, Projector augmented-wave method, *Phys. Rev. B* 50 (1994) 17953.
- [55] E.D. Wagner, M.J. Plewa, CHO cell cytotoxicity and genotoxicity analyses of disinfection by-products: an updated review, *J. Environ. Sci.* 58 (2017) 64–76.
- [56] M.J. Plewa, E.D. Wagner, W.A. Mitch, Comparative mammalian cell cytotoxicity of water concentrates from disinfected recreational pools, *Environ. Sci. Technol.* 45 (2011) 4159–4165.
- [57] S.-Q. Chen, Y. Shao, M.-T. Cheng, K.-F. Yao, Effect of residual stress on azo dye degradation capability of Fe-based metallic glass, *J. Non-Cryst. Solids* 473 (2017) 74–78.
- [58] Z. Jia, Q. Wang, L. Sun, Q. Wang, L.C. Zhang, G. Wu, J.H. Luan, Z.B. Jiao, A. Wang, S.X. Liang, Attractive in situ self-reconstructed hierarchical gradient structure of metallic glass for high efficiency and remarkable stability in catalytic performance, *Adv. Funct. Mater.* 29 (2019) 1807857.
- [59] F. Chen, L.L. Liu, J.J. Chen, W.W. Li, Y.P. Chen, Y.J. Zhang, J.H. Wu, S.C. Mei, Q. Yang, H.Q. Yu, Efficient decontamination of organic pollutants under high salinity conditions by a nonradical peroxymonosulfate activation system, *Water Res.* 191 (2021) 116799.
- [60] C.R. Cao, K.Q. Huang, J.A. Shi, D.N. Zheng, W.H. Wang, L. Gu, H.Y. Bai, Liquid-like behaviours of metallic glassy nanoparticles at room temperature, *Nat. Commun.* 10 (2019) 1–8.
- [61] X. Li, X. Liang, Z. Zhang, J. Ma, J. Shen, Cold joining to fabricate large size metallic glasses by the ultrasonic vibrations, *Scr. Mater.* 185 (2020) 100–104.
- [62] X. Liang, X.L. Zhu, X. Li, R.D. Mo, Y.J. Liu, K. Wu, J. Ma, High-entropy alloy and amorphous alloy composites fabricated by ultrasonic vibrations, *Sci. China: Phys., Mech. Astron.* 63 (2020) 116111.
- [63] Q.Q. Wang, M.X. Chen, P.H. Lin, Z.Q. Cui, C.L. Chu, B.L. Shen, Investigation of FePC amorphous alloys with self-renewing behaviour for highly efficient decolorization of methylene blue, *J. Mater. Chem. A* 6 (2018) 10686–10699.
- [64] R. Sahingoz, M. Erol, M.R.J. Gibbs, Observation of changing of magnetic properties and microstructure of metallic glass Fe<sub>78</sub>Si<sub>9</sub>B<sub>13</sub> with annealing, *J. Magn. Magn. Mater.* 271 (2004) 74–78.
- [65] Q.Q. Wang, M.X. Chen, L.L. Shao, Y.W. Ge, P.H. Lin, C.L. Chu, B.L. Shen, Effects of structural relaxation on the dye degradation ability of FePC amorphous alloys, *J. Non-Cryst. Solids* 525 (2019) 119671.